The Astrophysical Journal, 754:104 (22pp), 2012 August 1 doi:10.1088/0004-637X/754/2/104

THE *SPITZER* SURVEY OF INTERSTELLAR CLOUDS IN THE GOULD BELT. V. OPHIUCHUS NORTH OBSERVED WITH IRAC AND MIPS

J. Hatchell[1], S. Terebey[2], T. Huard[3,4], E. E. Mamajek[5,14], L. Allen[6], T. L. Bourke[7], M. M. Dunham[8], R. Gutermuth[9],
P. M. Harvey[10], J. K. Jørgensen[11], B. Merín[12], A. Noriega-Crespo[13], and D. E. Peterson[7]
[1] Astrophysics Group, Physics, University of Exeter, Exeter EX4 4QL, UK; hatchell@astro.ex.ac.uk
[2] Department of Physics and Astronomy PS315, 5151 State University Drive, California State University at Los Angeles,
Los Angeles, CA 90032, USA; sterebe@calstatela.edu
[3] Department of Astronomy, University of Maryland, College Park, MD 20742, USA
[4] Columbia Astrophysics Laboratory, Columbia University, New York, NY 10027, USA; thuard@astro.umd.edu
[5] Department of Physics & Astronomy, University of Rochester, P.O. Box 270171, Rochester, NY 14627-0171, USA; emamajek@pas.rochester.edu
[6] National Optical Astronomy Observatory, 950 North Cherry Avenue, Tucson, AZ 85719, USA; lallen@noao.edu
[7] Harvard-Smithsonian Center for Astrophysics, Cambridge, MA 02138, USA; tbourke@cfa.harvard.edu
[8] Department of Astronomy, Yale University, Box 208101, New Haven, CT 06520-8101, USA; michael.dunham@yale.edu
[9] Department of Astronomy, University of Massachusetts, Amherst, MA 01002, USA; rgutermu@astro.umass.edu
[10] Astronomy Department, University of Texas, Austin, TX 78712, USA; pmh@astro.as.utexas.edu
[11] Niels Bohr Institute and Centre for Star and Planet Formation, University of Copenhagen, Juliane Maries Vej 30, DK-2100 Copenhagen Ø, Denmark; jeskj@nbi.dk
[12] Herschel Science Centre, European Space Astronomy Centre (ESA), P.O. Box 78, 28691 Villanueva de la Cañada, Madrid, Spain; Bruno.Merin@sciops.esa.int
[13] Science Center, MC 220-6, California Institute of Technology, Pasadena, CA 91125, USA; alberto@ipac.caltech.edu
Received 2011 November 2; accepted 2012 May 27; published 2012 July 13

ABSTRACT

We present *Spitzer* IRAC (2.1 deg^2) and MIPS (6.5 deg^2) observations of star formation in the Ophiuchus North (Oph N) molecular clouds. This fragmentary cloud complex lies on the edge of the Sco–Cen OB association, several degrees to the north of the well-known ρ Oph star-forming region, at an approximate distance of 130 pc. The Oph N clouds were mapped as part of the *Spitzer* Gould Belt project under the working name "Scorpius." In the regions mapped, selected to encompass all the cloud with visual extinction $A_V > 3$, 11 young stellar object (YSO) candidates are identified, 8 from IRAC/MIPS color-based selection and 3 from Two Micron All Sky Survey (2MASS) K_S/MIPS colors. Adding to one source previously identified in L43, this increases the number of YSOcs identified in Oph N to 12. During the selection process, four color-based YSOcs were rejected as probable asymptotic giant branch stars and one as a known galaxy. The sources span the full range of YSOc classifications from Class 0/1 to Class III, and starless cores are also present. Twelve high extinction ($A_V > 10$) cores are identified with a total mass of $\sim$100 $M_\odot$. These results confirm that there is little ongoing star formation in this region (instantaneous star formation efficiency <0.34%) and that the bottleneck lies in the formation of dense cores. The influence of the nearby Upper Sco OB association, including the 09V star ζ Oph, is seen in dynamical interactions and raised dust temperatures but has not enhanced levels of star formation in Oph N.

Key words: circumstellar matter – infrared: stars – stars: evolution – stars: formation

Online-only material: color figures

1. INTRODUCTION

The Ophiuchus North (Oph N) molecular clouds lie 20° above the Galactic plane in the direction of the Galactic center. They are part of the same filamentary cloud complex as the well-studied Ophiuchus L1688 and L1689 clouds, but lie several degrees to the north, on the boundary of the constellation of Ophiuchus with Scorpius. Like the Ophiuchus L1688 and L1689 clouds, they are illuminated from the northwest by the Upper Scorpius (Upper Sco) subgroup of the Sco–Cen OB association.

The region has been studied little. Early low-resolution CO mapping (de Geus et al. 1990; de Geus 1992) showed the filamentary structure of the clouds in the Ophiuchus region (mirrored in the extinction maps published by Dobashi et al. 2005 and Rowles & Froebrich 2009) and suggested a shock origin due to expanding shells surrounding the Upper Sco subgroup. A detailed study of the molecular clouds was made in ^{13}CO by Nozawa et al. (1991) which gives an excellent overview of the cloud complex and its relationship to the Ophiuchus cores, *IRAS* sources, and the Sco–Cen OB association. They find that the region contains some 23 ^{13}CO clouds containing 51 ^{13}CO cores, with a total mass of 4000 $M_\odot$ and typical core densities of $N_{\mathrm{H}_2} \sim 3 \times 10^3$ cm^{-3}. The dense cores ($N_{\mathrm{H}_2} \sim 10^4$ cm^{-3}) and velocity structure were subsequently followed up in C^{18}O by Tachihara et al. (2000a, 2000b, 2002). Nozawa et al. (1991) identify only 13 young stellar objects (YSOs) associated with the cores, pointing to a low star formation efficiency of 0.3%.

Distance estimates for the Oph N molecular cloud complex come from its relationship with the stars in Upper Sco as, from extinction, the molecular clouds lie in front of and distributed through the OB population (de Geus et al. 1989). *Hipparcos* parallaxes place Upper Sco at a mean distance of 145 ± 2 pc (de Zeeuw et al. 1999), with a line-of-sight extent of ±17 pc assuming that the 14° spatial extent is reproduced in the third dimension. This places an effective upper limit on the clouds' distances of 162 pc. Extinction-based distance modulus estimates suggest that the clouds are distributed between 80 pc (near side) and 170 pc (far side), center 125 pc (de Geus et al. 1989) or, slightly farther away, 120 pc (near side) to 200 pc (far side; Straizys 1984). These distances are consistent with the *Hipparcos* data. Looking at individual stars, de Geus

---

[14] Current address: Cerro Tololo Inter-American Observatory, Cassilla 603, La Serena, Chile.

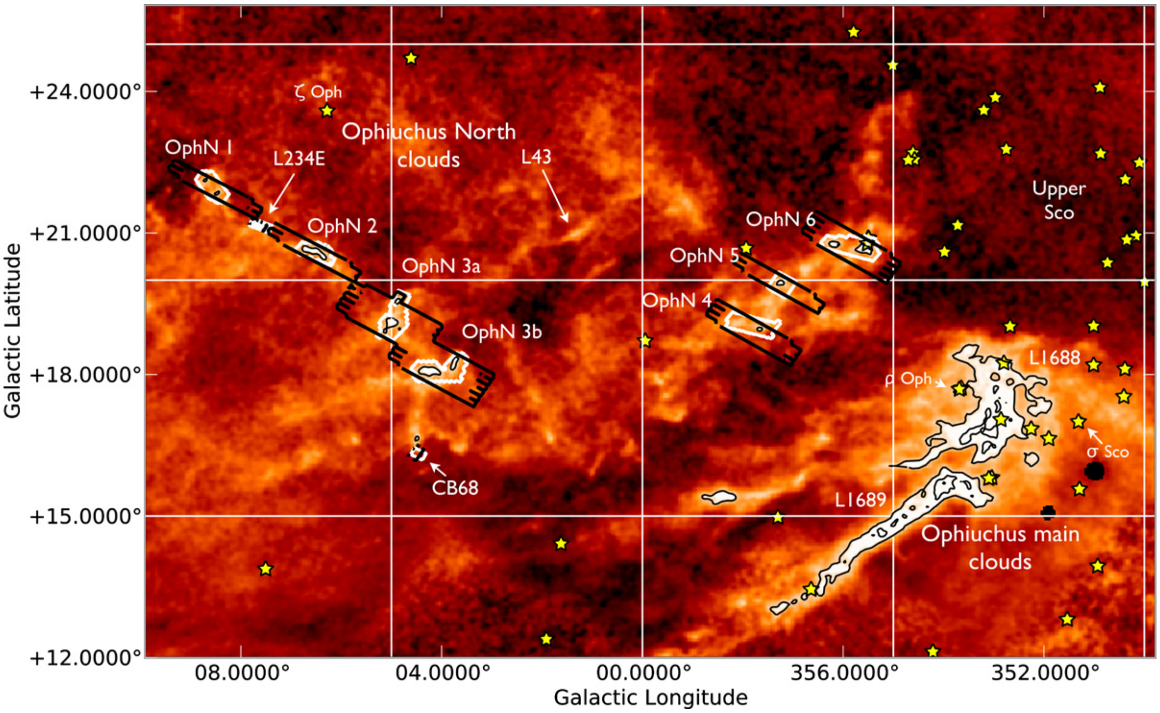

Figure 1. Regions observed by IRAC (white boxes) and MIPS (black boxes) overlaid on visual extinction from Dobashi et al. (2005). Extinction contours are at $A_V = 3$ and 6. OB stars associated with Upper Sco are marked by star symbols (Mamajek 2008).

(A color version of this figure is available in the online journal.)

et al. (1990) suggest that the western clouds (our OphN 4, 5, 6, their Complex 2) lie in front of χ Oph (150 pc) and the northeastern (OphN 1/2, Complex 4) in front of ξ Oph (130 pc). Recent estimates for the better-studied L1688 Ophiuchus cloud range from 120 to 145 pc (Wilking et al. 2008). There is certainly no reason to believe that the Ophiuchus clouds all lie at the same distance, but for convenience we assume a working distance of 130 pc, which is consistent with the above estimates.

In this paper, we present mid-infrared, *Spitzer Space Telescope* observations of the high column density regions of Oph N. The observations and data reduction are described in Section 2. Results, including source statistics, YSOcs, extinction maps, and large-scale emission, are given in Section 3 with comments on individual regions in the Appendix. The results are discussed in Section 4 and summarized in Section 5.

2. DESCRIPTION OF OBSERVATIONS

We observed Oph N in the mid-infrared as part of the *Spitzer* legacy program "Gould's Belt: star formation in the solar neighborhood" (SGBS). The clouds were mapped under the working name "Scorpius" (Sco) and appear under this name in the SGBS catalogs. We present them here as the Oph N clouds in line with previous nomenclature (Nozawa et al. 1991; Tachihara et al. 2000a, 2000b, 2002) which reflects their location predominantly within the constellation of Ophiuchus. Only our regions OphN 5, 6, and LDN 43 lie beyond the constellation boundary in Scorpius.

The SGBS program aimed to complete the mapping of local star formation started by the *Spitzer* "From Molecular Cores to Planet-forming Disks" (c2d) project (Evans et al. 2003, 2009) by targeting the regions IC5146, CrA, Scorpius (renamed Ophiuchus North), Lupus II/V/VI, Auriga, Cepheus Flare, Aquila (including Serpens South), Musca, and Chameleon to the same sensitivity and using the same reduction pipeline (Gutermuth et al. 2008; Harvey et al. 2008; Kirk et al. 2009; Peterson et al. 2011; Spezzi et al. 2011). Images were made at 3.6/4.5/5.8/8.0 μm with the Infrared Array Camera (IRAC; Fazio et al. 2004) and 24, 70 and 160 μm with the Multiband Imaging Photometer for *Spitzer* (MIPS; Rieke et al. 2004). With an 85 cm mirror, IRAC observes with an angular resolution of $2''$ whereas MIPS is diffraction limited with $6''$, $18''$, and $40''$ resolution at 24, 70, and 160 μm, respectively. For our observations, we targeted small regions encompassing the $A_V > 3$ contours from the optical extinction map of Dobashi et al. (2005), as shown in Figure 1. The area in Oph N which lies above $A_V > 3$ is fragmentary and scattered over an area of 20 deg^2. Some of these regions (L158, L204, L146/CB68, L234E, L260, L43) had already been mapped as part of the *Spitzer* "Cores to Disks" project (Evans et al. 2003). These were avoided by the *Spitzer* Gould Belt team to avoid unnecessary duplication of observations, as the two projects work to the same target sensitivities. Most of these c2d data are incorporated in this study of Oph N. The exception is L43 which is presented separately by Chen et al. (2009). Ultimately, seven new areas were mapped by SGBS with IRAC and MIPS. The Dobashi et al. (2005) and Rowles & Froebrich (2009) extinction maps, which are not limited to the IRAC observations but extend across the entire area covered by MIPS, confirm that all $A_V > 3$ (measuring from Dobashi et al. 2005) or $A_V > 4$ (Rowles & Froebrich 2009) regions in these filaments were observed by IRAC with the exception of two small clouds $0\overset{\circ}{.}3$ to the south of OphN 6 (included in the MIPS map) and $0\overset{\circ}{.}4$ to the north of CB68 (Tachihara et al. 2000b, core q2). Details of the data sets included for each region are listed in Table 1, including the observation dates, Astronomical Observation Request (AOR) identification numbers, program identification (30574 for *Spitzer* Gould Belt, 139 for "Cores to Disks"), and duration. Table 2 gives the associated Lynds Dark

Table 1
AORs in the *Spitzer* Gould Belt Oph N (Scorpius) Catalog

Instrument	R.A. (J2000)	Decl. (J2000)	PID	Duration (minutes)	Observation Date (yyyy-mm-dd)/Time	AOR Key
OphN 6						
IRAC	16:21:24.19	−19:56:01.80	30574	67.19	2007-09-09 03:51:06.6	19992320
IRAC	16:21:24.48	−19:56:05.80	30574	67.18	2007-09-09 07:49:28.5	19991808
MIPS	16:21:29.60	−19:57:45.00	30574	57.96	2007-04-08 18:13:07.4	20001280
MIPS	16:21:29.60	−19:57:45.00	30574	57.96	2007-04-09 00:39:24.0	20000768
OphN 5						
IRAC	16:27:45.78	−19:24:43.00	30574	25.38	2006-09-21 13:19:07.2	19960064
IRAC	16:27:45.78	−19:24:43.00	30574	25.38	2006-09-21 17:17:44.2	19959552
MIPS	16:27:40.00	−19:25:22.00	30574	30.83	2007-04-08 10:55:48.0	19968512
MIPS	16:27:40.00	−19:25:22.00	30574	30.83	2007-04-08 15:39:59.8	19968000
OphN 4						
IRAC	16:31:53.68	−19:35:03.00	30574	54.31	2006-09-21 12:12:25.1	19990784
IRAC	16:31:53.97	−19:35:07.00	30574	54.32	2006-09-21 16:27:39.8	19990272
MIPS	16:32:21.50	−19:43:36.10	30574	44.37	2007-04-06 23:54:22.0	19999744
MIPS	16:32:21.50	−19:43:36.10	30574	44.37	2007-04-07 05:44:06.0	19998976
OphN 3 (including c2d L158)						
IRAC	16:50: 6.45	−15:29:48.50	30574	68.54	2006-09-26 15:36:32.5	19959296
IRAC	16:50: 6.83	−15:29:47.80	30574	68.54	2006-09-26 22:11:19.0	19959040
MIPS	16:49:60.00	−15:30: 9.70	30574	78.19	2007-04-07 20:15:50.3	19966720
MIPS	16:49:60.00	−15:30: 9.70	30574	78.19	2007-04-08 04:12:25.9	19966208
IRAC	16:49: 4.02	−14:11:09.10	30574	48.44	2006-09-26 20:52:06.4	19990016
IRAC	16:49: 4.40	−14:11:08.40	30574	48.44	2006-09-27 00:51:11.2	19989504
MIPS	16:48:53.60	−14: 5:45.00	30574	78.19	2007-04-08 19:09:17.5	19996160
MIPS	16:48:53.60	−14: 5:45.00	30574	78.19	2007-04-09 01:35:34.1	19995904
IRAC	16:47:08.00	−13:58: 5.00	139	13.81	2004-08-16 18:55:38.5	5126400
IRAC	16:47:08.00	−13:57:55.00	139	13.81	2004-08-17 07:35:56.5	5126912
MIPS	16:47:15.60	−13:59:28.80	139	20.46	2005-03-10 02:36:55.6	9415680
MIPS	16:47:16.40	−13:56:41.20	139	20.46	2005-03-10 09:47:39.7	9427456
OphN 2 (including c2d L204C)						
IRAC	16:47:32.48	−12:06:21.40	30574	32.86	2006-09-23 01:45:10.0	19958784
IRAC	16:47:32.85	−12:06:20.60	30574	32.87	2006-09-23 06:07:36.2	19958528
MIPS	16:47:33.80	−12:09:06.40	30574	30.82	2007-04-08 10:26:38.9	19964160
MIPS	16:47:33.80	−12:09:06.40	30574	30.82	2007-04-08 15:10:50.8	19963904
IRAC	16:47:39.00	−12:21:09.00	139	8.49	2004-08-17 07:47:01.5	5127424
IRAC	16:47:39.00	−12:20:59.00	139	8.49	2004-08-18 05:38:13.0	5127936
MIPS	16:47:42.30	−12:21:11.70	139	20.39	2005-03-10 02:18:26.2	9408512
MIPS	16:47:35.70	−12:21:06.30	139	20.39	2005-03-10 09:29:20.8	9422080
OphN 1						
IRAC	16:47:24.26	−9:46:39.40	30574	43.07	2006-09-23 18:42:25.8	19988224
IRAC	16:47:24.63	−9:46:38.60	30574	43.07	2006-09-24 01:31:23.5	19987712
MIPS	16:47:24.01	−9:52:44.60	30574	30.82	2007-04-08 17:43:41.6	19994368
MIPS	16:47:24.01	−9:52:44.60	30574	30.82	2007-04-08 23:11:15.0	19994112
L234E						
IRAC	16:48:09.00	−10:55:56.00	139	12.05	2004-08-17 07:53:06.1	5128448
IRAC	16:48:09.00	−10:55:46.00	139	12.04	2004-08-18 05:44:20.5	5128960
IRAC	16:48:12.20	−10:55:59.60	139	20.39	2005-03-10 02:00:09.4	9411072
IRAC	16:48:05.80	−10:55:52.40	139	20.39	2005-03-10 09:10:57.7	9431808
L146/CB68						
IRAC	16:57:20.50	−16:09:02.00	139	8.83	2004-08-17 08:23:08.3	5130752
IRAC	16:57:20.50	−16:08:52.00	139	8.83	2004-08-18 07:55:40.2	5131264
MIPS	16:57:20.10	−16:10:25.80	139	18.87	2005-04-04 05:55:18.0	9425408
MIPS	16:57:20.90	−16:07:38.20	139	18.88	2005-04-05 22:55:58.5	9439232

Note. The original AOR names of regions OphN 1–6 were Sco 1–6.

Clouds (Lynds 1962) and molecular cores (C^{18}O; Tachihara et al. 2000a) for each region.

The overlap area covered in all four IRAC bands is slightly smaller than the area covered in any single band because the array design leads to an offset between the 3.6/5.8 μm and 4.5/8.0 μm maps. The final area covered by MIPS is much larger than with IRAC because of the long MIPS scans, with almost all the IRAC areas covered by MIPS as shown in Figure 1. In total, 2.1 deg^2 were covered by IRAC and 6.5 with MIPS. This is roughly half the area of 14.4 deg^2

Table 2
Associations with Lynds Dark Nebulae and Molecular Cores

Region	CO[a]	LDN (Opacity)[b]
OphN 1	U, u1, u2	L260 (6), L255 (6)
L234E	T, t	L234 (3)
OphN 2	S, s1–5	L204 (6)
OphN 3a	R, r1, r2	L152 (3), L158 (6), L162(6), L163(2), L141 (5), L137 (4)
OphN 3b	P, p1, p2	. . .
CB68	Q, q1	L146 (5)
OphN 4	C,–	L1757 (6)
OphN 5	C,–	L1752 (4)[c]
OphN 6	A, B, a, b	L1719 (5)[c]

Notes.
[a] Cores identified from ^{13}CO/C^{18}O (Tachihara et al. 2000b).
[b] Lynds Dark Nebula (Lynds 1962).
[c] Dark Nebulae L1719 and L1752 lie in the constellation of Scorpius, whereas all the others listed here are within Ophiuchus.

covered by MIPS in the main Ophiuchus clouds (Padgett et al. 2008).

The observations of each area were split between two epochs to allow the removal of transient objects, with the second epoch maps offset from the first epoch maps so that bad pixels do not always lie in the same sky positions. The IRAC observations were taken with a total integration time of 48 s per point, split equally between the two epochs, and an offset of 10″ in array coordinates between epochs. Short integrations in high dynamic range (HDR) mode were also taken for all regions in which bright YSOs were expected (the exception was L234E). The SGBS MIPS observations were taken in fast-scanning mode, stepping by 240″ cross-scan to fill gaps in the coverage, and (125″, 80″) between the two epochs in order to provide full 70 μm coverage with only half the array working. MIPS total integration times were 32.4 s at 24 and 70 μm and 6.2 s at 160 μm. The "Cores to Disks" observations of the small cores L234E and CB68 were taken in MIPS photometry mode. Each core was observed in two epochs. At 24 μm one cycle of 3 s was taken at each epoch for a total integration time of 84 s. At 70 μm three cycles of 3 s were taken at each epoch for a total integration time of ∼94 s.

2.1. Data Reduction

Data reduction was carried out using the c2d pipeline as described in the delivery documentation (Evans et al. 2007; see also Harvey et al. 2006; Rebull et al. 2007 for details of IRAC and MIPS processing). The basic calibrated data (BCD) from the Spitzer Science Center (SSC) were processed by the SGBS team to remove artifacts (e.g., bad pixels, jailbar effects, muxbleed column pull down due to bright sources) and apply the location-dependent photometric corrections.

2.1.1. Mosaics

Mosaicking was carried out using the SSC "Mopex" code. For IRAC mosaics, the HDR data were included in the final map, which improves the dynamic range and allows for the inclusion of otherwise saturated sources at the expense of slightly increased noise levels. For both IRAC and MIPS, both epochs were combined.

The SGBS Oph N data were reduced to form six separate maps, numbered OphN 1–OphN 6 in order of decreasing Galactic longitude. These were originally mapped as Sco 1–6 but relabeled "OphN" in line with the overall cloud nomenclature change. OphN 1, 4, 5, and 6 each incorporated a single SGBS AOR area. For OphN 2, the c2d cloud L204C was mosaicked with the SGBS data. For OphN 3, the MIPS observations for two of the SGBS regions and the overlapping c2d region L158 were merged into a single mosaic. The IRAC observations for OphN 3 remain split into OphN 3a (including L158) and OphN 3b. The two separate c2d cores L234E and CB68 were mosaicked individually. These pairings are indicated in Table 1. A finding chart showing the six SGBS regions and the two complementary c2d areas overlaid on the Dobashi et al. (2005) extinction map is shown in Figure 1.

2.1.2. Catalogs

Source extraction was carried out in each of the four IRAC bands on the combined mosaics (two epoch plus HDR), plus MIPS 24 μm on the combined epoch mosaics, using c2dphot, a photometry tool based on DoPHOT (Harvey et al. 2006; Schechter et al. 1993). Sources believed to be real at one or more wavelengths were bandfilled at the missing wavelengths, first in IRAC bands 1–4 then MIPS 24 μm then MIPS 70 μm by fitting a point spread function (PSF) to images at the missing wavelengths, and these fluxes are included in the catalogs with bandfilling noted in the data quality flags. Fluxes were extracted from the 2MASS point-source catalog (Skrutskie et al. 2006) using a 2″ position matching criterion. The 70 μm source list was separately matched to the shorter wavelength catalog with an 8″ position matching criterion. With a larger pixel size of 10″ at 70 μm (compared to 1.″2 for IRAC and 2.″55 at 24 μm) sources often matched more than one shorter-wavelength source. The 70 μm fluxes were assigned to the best candidate by hand matching the spectral energy distribution (SED), with the remaining possible 70 μm emitters also noted in the catalog. Source matching was not attempted at 160 μm as the spatial resolution is low at this wavelength (∼40″) and most bright regions are saturated. For further details on source extraction see the c2d delivery documentation (Evans et al. 2007).

2.1.3. 160 μm Data

The 160 μm data obtained in fast-scan mode mapping do not have enough redundancy to fill in completely all the gaps due to a dead readout and the intermediate gap between the array detector rows (MIPS Instrument Support Teams 2007). Furthermore, with only two epochs, effectively two pointings per pixel, the effects of hard radiation hits and saturation translate into small regions without data. To deal with these gaps and to preserve as much as possible of the diffuse emission, the images are first resampled from 15″ to 8″ pixels and then a 5 pixel by 5 pixel median filter is applied to the image. The net effect is a slight redistribution of surface brightness (∼15%) and smearing of the original beam from 40″ to about 1′ in size. 160 μm data are not available for the two c2d cores CB68 and L234E.

Fluxes at 160 μm are determined using aperture photometry with a 32″ radius aperture, an annulus from 64″ to 128″, and an aperture correction of 1.97. Flux density uncertainties are about 20% below 5 Jy and 30% for higher flux densities (Rebull et al. 2010). Visual inspection of each 160 μm source in the original unsmoothed image is used to determine whether the object is cleanly detected or contaminated by data dropouts.

Table 3
Detection Statistics with IRAC and 2MASS

Detection Type	Detections
At least one IRAC band	106200
All four bands	5378
Only three bands	7902
Only two bands	50632
Only one band	42288
MIPS 1	845
MIPS 1 and IRAC	762
MIPS and all four IRAC bands	449
2MASS k	10919
2MASS k and h	10822
2MASS k and at least one IRAC band	10917
2MASS k and all four IRAC bands	4723
2MASS k but not IRAC	2
IRAC band 1 but not 2MASS k	89038
MIPS, all four IRAC bands, and 2MASS k	196

Notes. Detections are counted above a signal-to-noise ratio of 3 and in the overlap area of all four IRAC bands only.

Table 4
Detection of Sources above Various S/N Thresholds in Individual IRAC Bands

S/N	3.6 (μm)	4.5 (μm)	5.8 (μm)	8.0 (μm)
3	136853	94166	18320	821
5	101913	64178	9618	5465
10	50565	28830	4742	2696
15	23182	13459	2446	1460

Notes. Sources are counted here even if they fall outside the four-band overlap area, so counts can be larger than in Table 3.

3. RESULTS

Red–green–blue (RGB) images for the eight Oph N regions mapped (OphN 1–6, CB68 and L234E) are shown in Figures 2 and 3. The first figure shows a combination of IRAC 3.6 μm (blue), 4.5 μm (green), and 8 μm (red), and the second combines IRAC 4.5 μm (blue), IRAC 8 μm (green), and MIPS 24 μm (red). The RGB images each cover the overlap region where data are available from all the three chosen *Spitzer* instruments, corresponding to the IRAC areas (white boxes) in Figure 1. The regions are irregular with sizes starting at 0.3 pc for CB68 and L234E, with OphN 3a the largest region mapped at a couple of parsecs in length; scale bars of 0.2 pc are shown on Figures 2 and 3.

Unextincted foreground stars appear blue–white in these images. Embedded protostars have redder colors, as do background galaxies, background giants, and planetary nebulae, extincted main-sequence stars, and foreground late-type stars (Robitaille et al. 2008). The red wisps of 8 μm emission are polycyclic aromatic hydrocarbon emission from heated clouds. Shocked H_2 emission from molecular outflows can show up at 4.5 μm in green on the IRAC three-color plot, but there is no evidence for this here.

Figures 2 and 3 show that there are no dense protostellar clusters in Oph N, such as *Spitzer* found in Serpens and Auriga (Gutermuth et al. 2008; B. Matthews & N. Tothill 2012, in preparation). The bright region in the southwest of OphN 6 is the optical reflection nebula IC4601 (Magakian 2003), excited by a few late-type B and A stars (see Appendix A.7). There is no dense young reddened cluster associated with these intermediate-mass stars, as Figure 3 shows. The YSOs associated with OphN 6 and other regions are discussed in Section 3.3.

3.1. Source Statistics

The Oph N IRAC and 2MASS source detection statistics are given in Table 3. In the area covered by all four IRAC bands, just over 100,000 sources were detected in at least one IRAC band with a signal-to-noise ratio (S/N) of at least 3, with more than 5000 detected in all four IRAC bands. Nearly all of the 2MASS sources in the field were also detected by IRAC, with half of these detected in all four IRAC bands. The number of sources detected as a function of the required S/N in the individual wavelength maps is given in Table 4. These counts include the entire region covered in each waveband and not solely the overlap area, which is why the 3.6 μm detection count for S/N = 3 is larger than in Table 3.

3.2. Background Sources

Most of the sources detected by *Spitzer* are expected to be either main-sequence stars or background galaxies. In order to estimate the fraction of young sources associated locally with the Oph N star-forming region, a comparison with the Wainscoat model for the Galactic stellar background at this latitude is made in Figure 4 (Wainscoat et al. 1992). The figure shows differential source counts for all sources in each of the four IRAC bands and MIPS1 from the Oph N catalog (gray curves for all sources; black curves for sources classified as stars with 3σ detections) compared to the Wainscoat predictions (dashed curve). For Oph N, most of the source detections are main-sequence stars, as shown by the lack of excess counts over the Wainscoat model in the IRAC bands. The excess in the MIPS band over the Wainscoat model is mainly due to background galaxies. The completeness limit at approximately 15 mag in the IRAC bands can be seen in the turnover in the star counts (black line).

3.3. YSO Candidates

The main aim of the SGBS program is to locate the YSOs associated with star formation. In the Oph N molecular clouds, 11 young stellar object candidates (YSOcs) were identified on the basis of their position in IRAC color–magnitude diagrams, as shown for each of the IRAC four-band detections in Figure 5. The selection process is described in detail in Harvey et al. (2007) but in summary, each color–magnitude diagram yields a probability of a source being a YSOc with the region occupied by galaxies, based on the SWIRE sample, giving a low probability. The individual probabilities are then combined with some additional criteria to separate the YSOcs (colored red) from galaxies. The method aims to eliminate background sources at the expense of also eliminating some YSOcs. This process is not infallible and follow-up visual inspection of the mosaics identified one extended and elliptical YSO candidate as a galaxy (6dFGS gJ164828.8−141437; Jones et al. 2006).

The remaining 10 YSOc were classified Class I, flat-spectrum, Class II, or Class III according to their spectral index fit between the K band (1.2 μm) and MIPS band 1 (24 μm) as listed in Table 5. Fluxes for these sources are listed in Table 6 and SEDs are shown in Figure 6. These include optical (B, V, R_C) magnitudes from the NOMAD catalog from a 5″ radius position search (Zacharias et al. 2005). For the more evolved sources, the SEDs are also shown dereddened to fit a stellar photosphere at the short wavelengths. The best wavelength/band for identifying

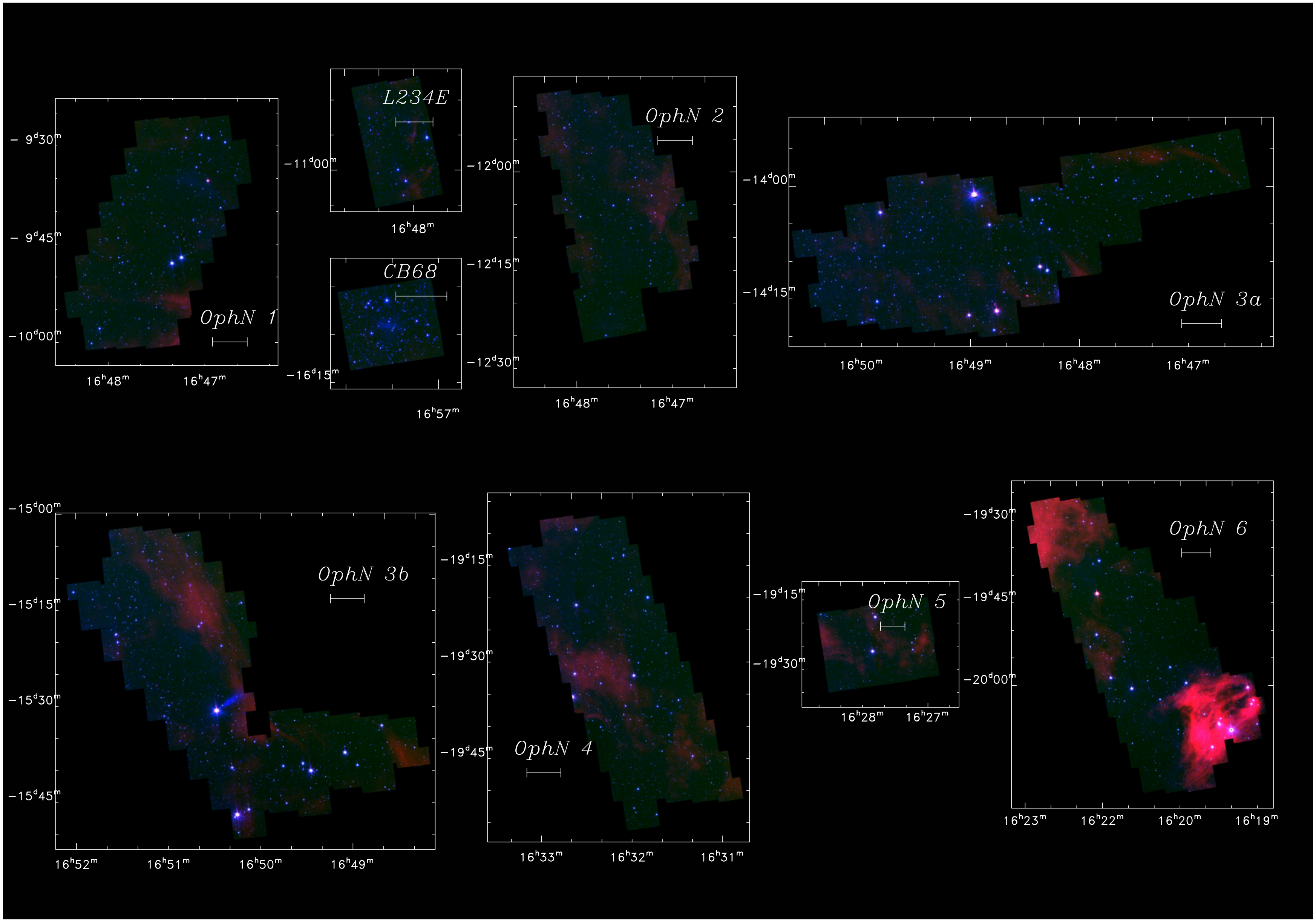

Figure 2. Three-color mosaics of the Oph N cloud regions imaged by *Spitzer* with IRAC 3.6 μm (blue), IRAC 4.5 μm (green), and IRAC 8.0 μm (red). Only the overlap regions imaged at all three wavelengths are shown. The scale bars represent 0.2 pc at the assumed distance of 130 pc.

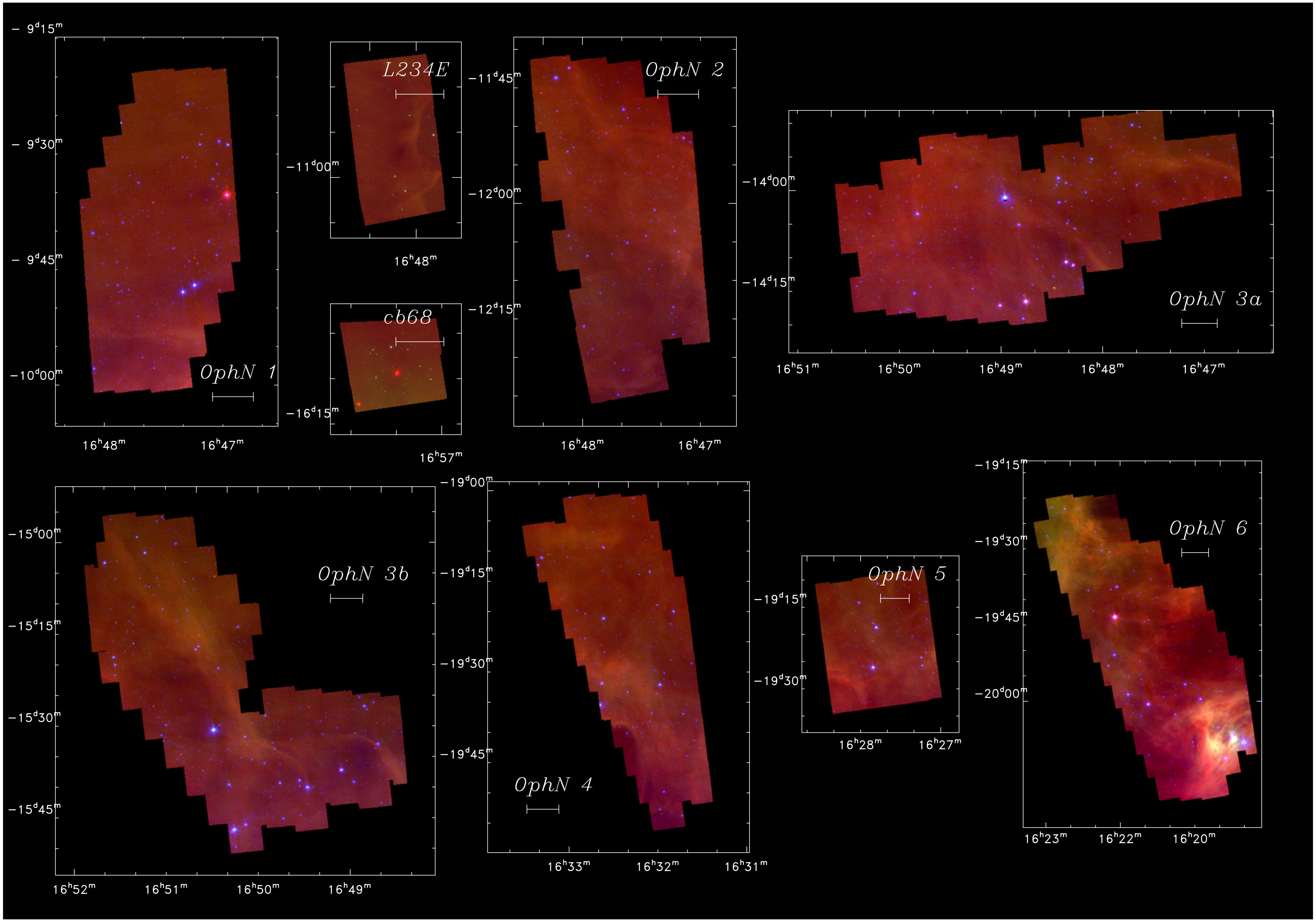

Figure 3. Three-color mosaics of the Oph N cloud regions imaged by *Spitzer* with IRAC 4.5 μm (blue), IRAC 8.0 μm (green), and MIPS 24 μm (red). Only the overlap regions imaged at all three wavelengths are shown. The scale bars represent 0.2 pc at the assumed distance of 130 pc.

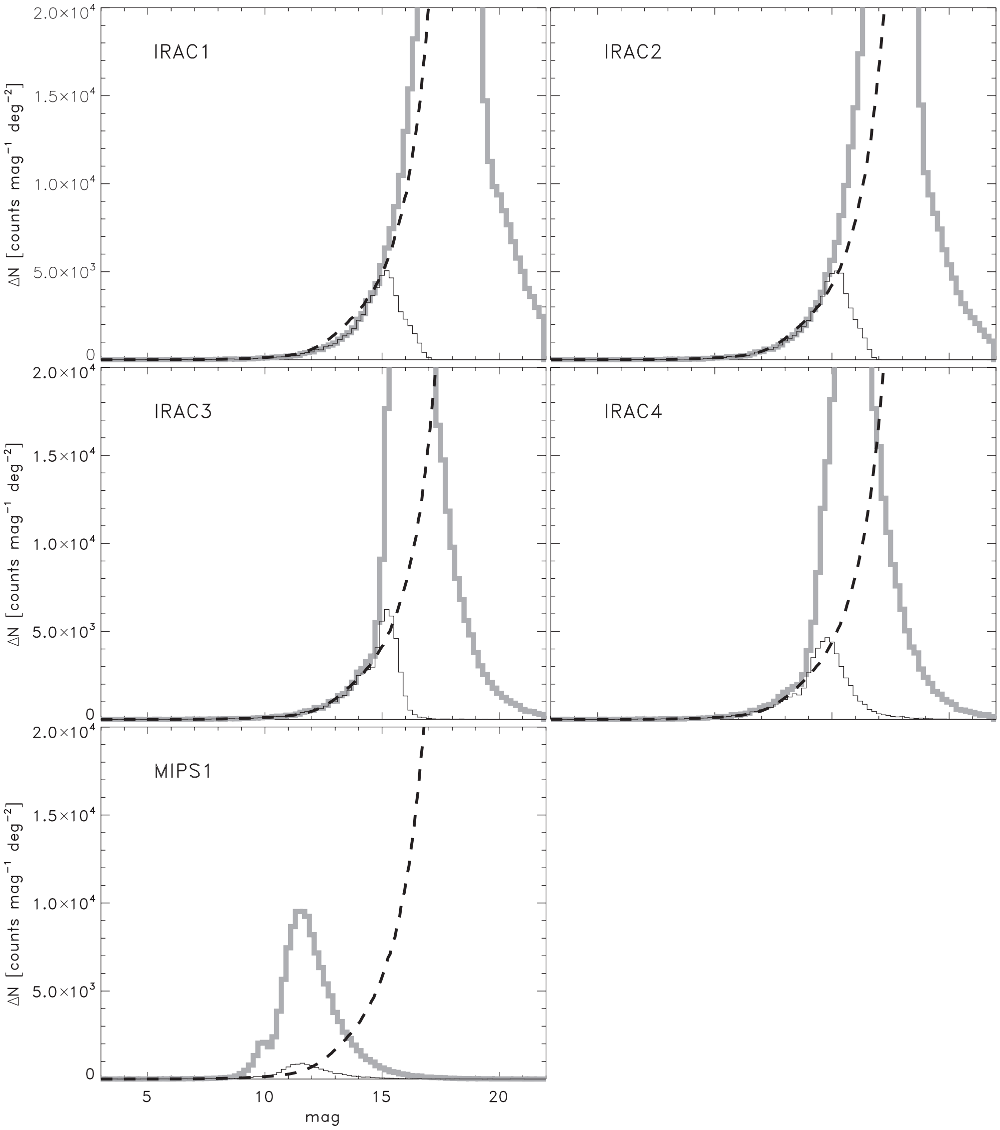

Figure 4. Differential source counts compared to the Wainscoat model for the galactic stellar background. The thick gray line shows the differential source counts per square degree in each band for all cataloged sources. The thin black line shows the differential source count for only the sources classified as stars. The stellar count can be compared to the dashed line which shows the Wainscoat model for the stellar density in the Galaxy.

Table 5
YSO Candidates with IRAC Detections

YSOc	SSTgbs	Field	Class	α[a]	ID (Offset)	Submm Core	References
1	J164658.3−093519	OphN1	I	0.66	IRAS 16442−0930 (0′.9)	L260 SMM1	1, 2, 3
2	J164817.6−141109	OphN3	II	−0.70	V2507 Oph(9″.0), Oph4 (9″.0)[b]		4, 5
3	J164821.9−141043	OphN3	II	−1.03	IRAS 16455−1405 (0″.27), PDS 91		1, 6
4	J164845.6−141636	OphN3	II	−0.97	IRAS 16459−1411, V2508 Oph, Oph6 (0″.16)	L162 SMM1	5, 7, 8
5	J164900.8−141711	OphN3	II	−1.28	Oph 5 (0″.12), HBC 654		5
6[c]	J164905.6−153713	OphN3	III	−1.87	IRAS 16462−1532 (7″.45)		
7[c]	J162137.7−200037	OphN6	III	−2.09	...		
8	J162204.3−194327	OphN6	F	0.02	IRAS 16191−1936 (1″.04)	L1719B	1, 2, 9
9	J162209.6−195301	OphN6	III	−2.11	...		
10	J165719.6−160923	CB68	I	2.40	IRAS 16544−1604 (12″.05)	CB68,CB68SMM1	10, 1, 11

Notes.

[a] Infrared spectral index α from a fit to fluxes from K_S band to MIPS 24 μm (Evans et al. 2007).

[b] The *Spitzer* detection and V2507 Oph are separate stars, probably in a binary. See Appendix A.4.

[c] Probably an AGB star. See Section 3.5.

References. (1) Carballo et al. 1992; (2) Bontemps et al. 1996; (3) Visser et al. 2001; (4) Ducourant et al. 2005; (5) André & Montmerle 1994; (6) Reipurth & Zinnecker 1993; (7) Andrews et al. 2009; (8) Visser et al. 2002; (9) Kirk et al. 2005; (10) Clemens & Barvainis 1988; (11) Huard et al. 1999.

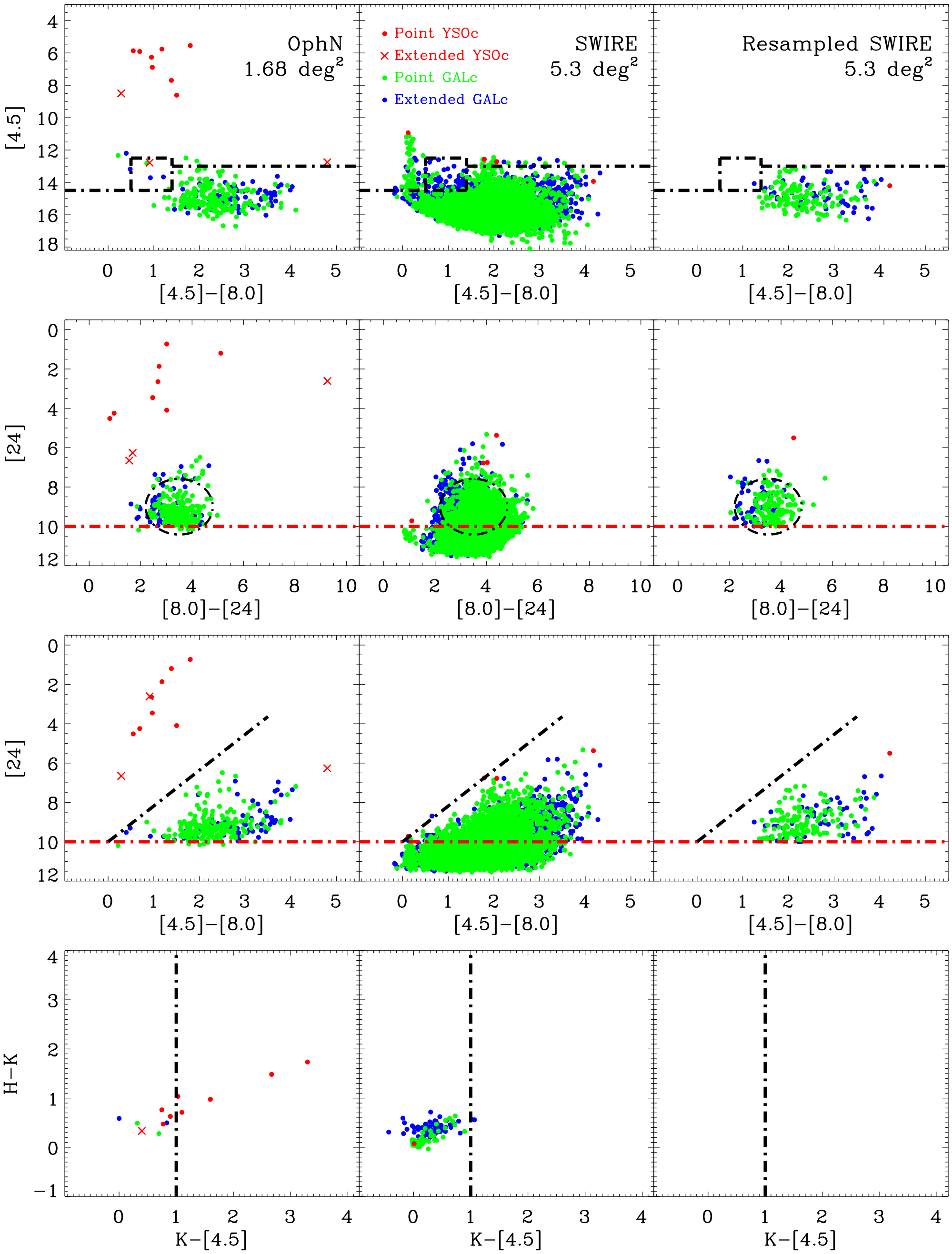

Figure 5. Color–magnitude diagrams for all Oph N regions combined, showing the YSOc identification criteria from Harvey et al. (2007) and Evans et al. (2007). Symbols are point-like/extended YSOcs (red circles/crosses) and point-like/extended galaxies (green/purple) as shown in the key. The black lines show the fuzzy color–magnitude cuts that define the YSO candidate criterion. Objects fainter than the hard limits shown as red dot-dashed lines are excluded from the YSOc category. The area covered is the 1.68 deg^2 covered by both IRAC and MIPS.

the continuum of stellar emission in these young objects is the *J* band, which was used to normalize the reddened photospheres to the SEDs. In all but two cases this was a K7 star, but for sources 3 and 4 an A0 star was needed in order to reproduce the high fluxes. These YSOc SEDs show disk excesses over a stellar photosphere at long wavelengths. The poor match between the SED and the optical data in some cases (YSOc 3, 6, 7) is most likely to be due to misassociations as several optical sources within the 5″ radius contribute to the SED of a single source in the *Spitzer* bands. Some of these sources could also have ultraviolet excesses due to disk accretion that prevent good fits to main-sequence stellar photosphere models (Calvet & Gullbring 1998). It is also possible that the reddening law in these dense cores could differ from the $R_V = 5.5$ Weingartner & Draine interstellar grain model (Weingartner & Draine 2001; Indebetouw et al. 2005), but this correction would be likely to be similar for all sources.

No photosphere is fitted to the flat-spectrum or Class I sources. These embedded YSOcs have emission peaking at longer wavelengths than main-sequence stars and can be identified by their redder colors in the RGB diagrams (Figures 2 and 3). The Class I sources in OphN 1 (YSOc 1) and CB68 (YSOc 10), and the flat-spectrum source in OphN 6 (YSOc 8), show up in this way.

More than half of the YSOcs were detected by *IRAS* and all but three were previously identified as YSOs (see Table 5).

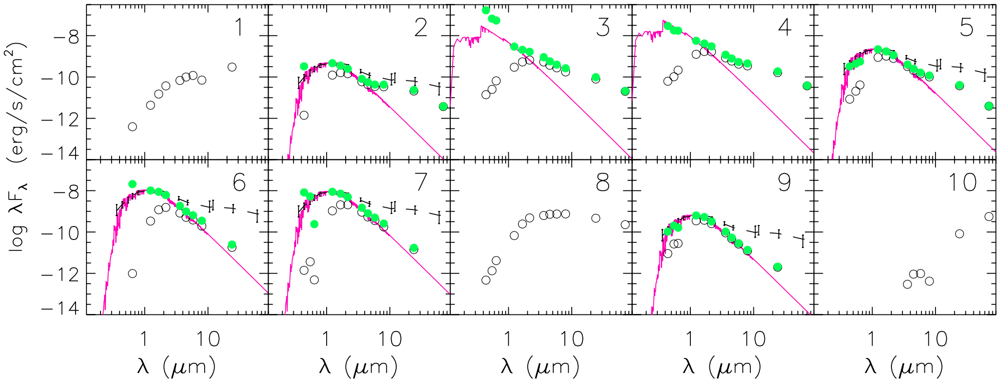

Figure 6. Spectral energy distributions for the 10 YSOcs listed in Table 5. Measured NOMAD, 2MASS, IRAC, and MIPS fluxes are shown as open circles. For the evolved sources (flat spectrum, Class II, and Class III), photospheric models are plotted for a K7 star except for sources 3 and 4 for which an A0 photosphere was used. The filled circles (green in the online version) then show the fluxes corrected for reddening. For the Class I sources 1 and 8, no photospheric model is plotted. The dashed line shows the median SED of T Tauri stars in Taurus (with error bars showing the quartiles of the distribution; Hartmann et al. 2005). Uncertainties are smaller than the symbol size (see Table 6).

(A color version of this figure is available in the online journal.)

Table 6
Fluxes for YSO Candidates with IRAC Detections

YSOc	2MASS			*Spitzer* IRAC				*Spitzer* MIPS		
	J (mJy)	*H* (mJy)	K_s (mJy)	F3.6 (mJy)	F4.5 (mJy)	F5.8 (mJy)	F8.0 (mJy)	F24 (mJy)	F70 (mJy)	F160 (mJy)
1	1.8 ± 0.1	8.3 ± 0.3	26.8 ± 0.8	81.8 ± 4.3	150.0 ± 7.8	231 ± 11	189 ± 12	2430 ± 248	...[a]	3700 ± 730
2	50.9 ± 1.7	90.4 ± 4.4	105.0 ± 2.6	71.4 ± 3.5	64.6 ± 3.1	68 ± 3	90 ± 4	168 ± 16	87 ± 12	<2200
3	123.0 ± 3.2	298.0 ± 7.7	477.0 ± 7.9	641.0 ± 31.9	559.0 ± 30.5	539 ± 26	471 ± 23	639 ± 59	476 ± 49	<2200
4	519.0 ± 11.5	957.0 ± 33.5	1200.0 ± 29.9	1010.0 ± 51.5	889.0 ± 46.0	816 ± 40	925 ± 44	1310 ± 124	873 ± 92	<2200
5	371.0 ± 8.2	571.0 ± 21.0	575.0 ± 11.1	390.0 ± 19.9	315.0 ± 19.1	274 ± 13	270 ± 13	303 ± 28	92 ± 14	<2200
6	140.0 ± 3.2	663.0 ± 25.6	1120.0 ± 21.8	1000.0 ± 51.6	778.0 ± 43.4	742 ± 36	517 ± 25	146 ± 14	<11	<2200
7	437.0 ± 8.4	1150.0 ± 38.2	1510.0 ± 25.0	1100.0 ± 57.9	809.0 ± 40.4	694 ± 34	472 ± 22	114 ± 11	<11	<2200
8	27.8 ± 0.7	136.0 ± 2.9	347.0 ± 8.3	759.0 ± 38.3	1090.0 ± 56.3	1440 ± 69	2010 ± 110	3730 ± 390	5320 ± 573	8700 ± 730
9	144.0 ± 3.8	208.0 ± 4.8	184.0 ± 4.1	109.0 ± 6.6	71.5 ± 4.1	50 ± 3	33 ± 2	16 ± 2	<11	<2200
10	0	0	0	0.4 ± 0.0	1.4 ± 0.1	1.9 ± 0.1	1.1 ± 0.1	659 ± 61	13100 ± 1210	...

Note. [a] Source lies outside the 70 μm map.

The two deeply embedded Class 0/I sources are the known protostars L260 SMM1 (André & Montmerle 1994; Visser et al. 2002) and CB68 (Carballo et al. 1992; Huard et al. 1999). Most of the Class II objects are T Tauri stars which have been the subject of multiple studies. The three new identifications are the Class III sources OphN YSO6, 7, and 9, identified through their small 24 μm excesses. Two of these (YSOc6 and 7) may be background asymptotic giant branch (AGB) stars; we examine this possibility in Section 3.5. OphN 7 and 9 both lie between the extinction peaks of OphN 6 (Figure 11). Finding pre-main-sequence stars in OphN 6 is unsurprising as it lies on the edge of the Sco–Cen association.

3.4. 24 μm Emission and MIPS-only YSO Candidates

A larger area of Oph N was covered by MIPS at 24, 70, and 160 μm and by 2MASS in the near infrared, but not at intermediate wavelengths by IRAC. YSOs in that region are not found on the standard IRAC-based color–magnitude diagrams as shown in Figure 5. A start on identifying YSOcs with no IRAC data can be made by looking for sources with red colors in 2MASS $K_S - [24]$.

The K_S versus $K_S - [24]$ color–magnitude diagram is shown in Figure 7, following Rebull et al. (2007; Perseus) and Padgett et al. (2008; Ophiuchus). All Oph N sources detected at

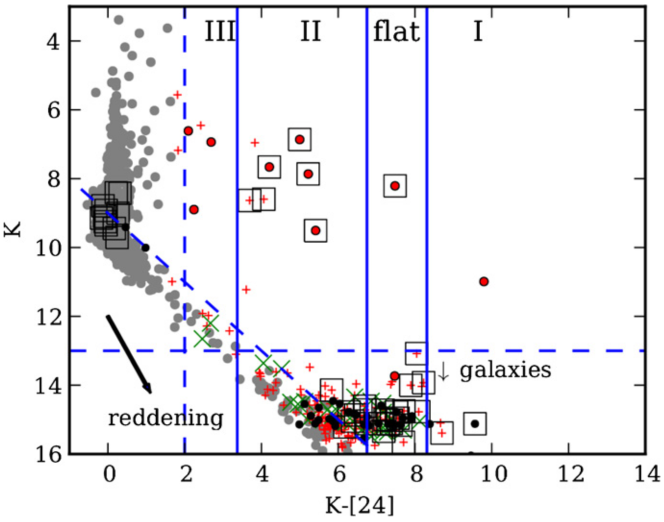

Figure 7. K_S vs. $K_S - [24]$ color–magnitude diagrams for all Oph N regions combined. Symbols reflect the c2d pipeline classification: stars (gray dots); star+dust (+, red in the online version); galaxies (×, green in the online version); YSOc (black circles, filled red in the online version); and other (black dots). Class III, Class II, flat-spectrum, and Class I source models and the horizontal and diagonal lines mark cuts for faint K_S and 24 μm detections.

(A color version of this figure is available in the online journal.)

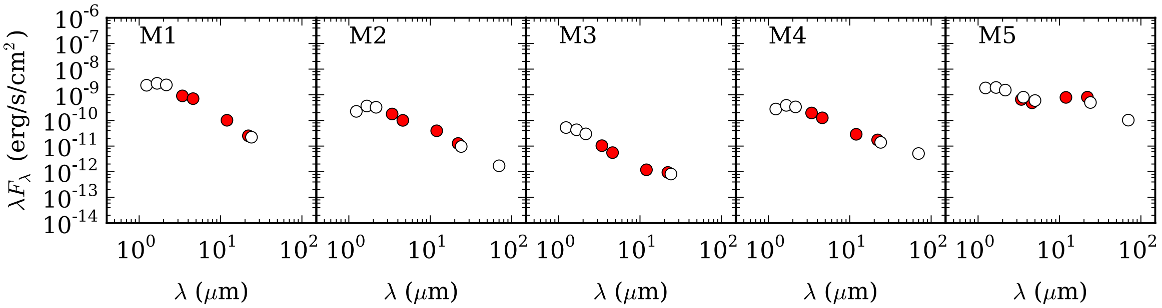

Figure 8. Spectral energy distributions for sources detected via K-24 μm colors (see Table 7). Fluxes from 2MASS and *Spitzer* are plotted as open circles and those from *WISE* as filled circles (red in the online version).

(A color version of this figure is available in the online journal.)

these wavelengths are included (OphN 1–6, CB68 and L234E combined). The source symbols are based on the c2d pipeline classification. To be classified as a YSOc requires fluxes in all four IRAC bands and MIPS1; red sources which do not fulfill this criterion (e.g., those not observed by IRAC) tend to be classified as "galc" or "star+dust" (Evans et al. 2007; see Section 2.1.2).

In Figure 7, sources with the colors of stellar photospheres appear to the left with $K_S - [24] < 2$, and most of the sources in this region are already classified as stars (gray circles) by SED fitting. A reddening vector is shown in the bottom left of the plot, assuming an extinction law of $A_{24}/A_{K_S} = 0.5$ as recommended by Chapman et al. (2009); however, the 24 μm relative extinction is quite uncertain. Reddened stars are likely to appear down and to the right of the main stellar population. The extinction in Oph N is low over most of the cloud, with only a small fraction above $A_V = 3$ (Figure 1 and Section 3.7), so few background stars should be reddened significantly, and indeed there are relatively few sources in this region. The lower left region of the diagram is not populated because stellar photospheres with $K_S > 10$ do not lie above the MIPS 24 μm sensitivity limit unless they are reddened.

Background galaxies ("Galc," green ×) typically have low K_S fluxes and lie toward the bottom of the plot, as shown by the colors of objects in the SWIRE catalog (Rebull et al. 2007; Padgett et al. 2008). In this region are found most of the c2d pipeline-classified "star+dust" sources (red +), which have the colors of a stellar photosphere but excess due to dust at the long wavelengths.

Candidate YSOs with $K_S - [24]$ excesses appear in the center of the plot, to the right of the stars, depending on the contribution of dust in the disk and/or envelope. This is where the ten "YSOc" already identified by the c2d pipeline and IRAC color–magnitude diagrams appear (red filled circles), with the exception of CB68, which was not detected by 2MASS (or IRAC1) and does not appear on this plot. In this region there are several additional YSOcs with no IRAC detection, currently classified "star+dust" (red plus symbols) due to their long-wavelength excess over a stellar photosphere.

At this point we make a selection for a clean sample of MIPS-only YSOcs, rejecting the regions of color–magnitude space with $K_S < 13$, which excludes the majority of background galaxies, $K_S - [24] > 2$, which excludes the background stars, and $[24] > 9$, which removes reddened stars. This is a conservative selection which probably rejects some genuine YSOs. We make the galaxy cut at $K_S = 13$ rather than $K_S = 14$ (Rebull et al. 2007; Padgett et al. 2008) because the two brightest sources below $K_S = 13$ in the flat-spectrum region of the plot both have galaxy identifications. The misclassified "YSOc," which has an IRAC detection and appears as a red filled circle, is 6dFGS gJ164828.8−141437 and the brighter $K_S \simeq 13$ source is 6dFGS gJ163139.8−202044.

The five MIPS-only YSOcs in Oph N selected by these criteria are listed in Table 7. We can classify them further based on the standard spectral index α calculated from $K_S - [24]$ into Class I, flat-spectrum, Class II, and Class III sources (Rebull et al. 2007; Greene et al. 1994); the corresponding regions of color space are identified on Figure 7. The three Class II candidates M5, M2, and M4, in OphN 3, 4, and 6, respectively, are close in color to the existing YSOcs and have strong K_S and 70 μm detections. The fainter K_S source M3 is also a Class II candidate in OphN 6. In OphN 3, the Class III source M1 which lies redward of the main stellar population is identified as IRAS 16484−1557.

To fill in the missing mid-IR portion of the spectrum for regions not covered by IRAC, additional mid-infrared fluxes were taken from the *WISE* Preliminary Release Source Catalog (Wright et al. 2010).[15] *WISE* provides fluxes at 3.4, 4.6, 12, and 22 μm with angular resolution of $6''$–$12''$. The resulting SEDs, shown in Figure 8, confirm the sources to be similar to the Class II/III YSOcs in Figure 6. The classification of the source M5 (V1121 Oph), which shows a strong disk excess, deserves some further comment. Aperture photometry with a $100''$ aperture gives a 24 μm flux an order of magnitude higher than the c2d pipeline (∼4000 rather ∼400 mJy) and the higher flux is confirmed by *WISE* at 22 μm (5915 ± 49 mJy; see Table 8). The higher 22/24 μm fluxes move this source to the Class II/flat-spectrum boundary (Figure 7).

$K_S - [24]$ alone is an imprecise selection tool, and there may be additional YSOs in the excluded regions, particularly among the faint 24 μm sources. Color–magnitude searches based on *WISE* data may be a way to identify these but are beyond the scope of this paper.

3.5. AGB Star Contamination

There remains the possibility that some of the YSOcs may be background AGB stars. Like YSOs, AGB stars have red colors due to the dust shells which surround them. They occupy a similar region in color–magnitude space to YSOcs and cannot easily be separated by the criteria shown in Figure 5 (Robitaille et al. 2008). As befits an old stellar population, AGB stars are distributed throughout the Galaxy with increased counts in the thick disk and bulge. Oph N lies 17°–24° from the plane, so using the Galactic distribution model from Ishihara et al. (2011)

---

[15] http://wise2.ipac.caltech.edu/docs/release/prelim/expsup/

Table 7
YSO Candidates Identified from MIPS 24 μm and 2MASS in Regions with No IRAC Coverage

YSOc	SSTgbs	Field	Class	ID (Offset)	References
M1[a]	J165121.4−160259	OphN3	III	IRAS 16484−1557 (7″), ASAS 165122−1602.9 (5″.9)	1
M2[a]	J163142.5−203814	OphN4	II		
M3	J162214.8−204540	OphN6	II		
M4	J162229.8−200248	OphN6	II	2RXP J162230.1−200256 (9″.1)	
M5[b]	J164915.3−142209	OphN3	II	V1121 Oph(0″.08)	2, 3

Notes.
[a] Probably an AGB star. See Section 3.5.
[b] V1121 Oph lies outside the IRAC mapping region at 4.5 and 8.0 μm so is not classified as a YSOc by the c2d pipeline.
References. (1) Pojmanski et al. 2005; (2) André & Montmerle 1994; (3) Carballo et al. 1992.

Table 8
Fluxes for YSO Candidates Identified from MIPS 24 μm and 2MASS

YSOc	2MASS			*WISE*				*Spitzer* MIPS		
	J (mJy)	*H* (mJy)	K_S (mJy)	F3.4 (mJy)	F4.6 (mJy)	F12 (mJy)	F22 (mJy)	F24 (mJy)	F70 (mJy)	F160 (mJy)
M1	969.0 ± 18.7	1550.0 ± 28.5	1750.0 ± 33.9	1029.7 ± 38.9	1086.9 ± 24.0	406.91 ± 7.12	185.34 ± 4.27	178 ± 17	<11	<2200
M2	93.1 ± 1.8	203.0 ± 3.9	235.0 ± 4.6	202.6 ± 2.4	154.7 ± 2.4	158.31 ± 2.62	93.06 ± 2.40	77 ± 7	40 ± 7	<2200
M3	21.8 ± 0.5	24.0 ± 0.6	21.6 ± 0.4	11.8 ± 0.3	8.5 ± 0.2	4.79 ± 0.21	6.92 ± 1.21	7 ± 1	<11	<2200
M4	115.0 ± 2.3	215.0 ± 4.2	243.0 ± 4.3	222.2 ± 4.9	194.2 ± 3.6	115.75 ± 1.92	128.10 ± 2.95	112 ± 10	120 ± 16	<2200
M5	762.0 ± 27.4	1070.0 ± 23.6	1100.0 ± 26.2	746.6 ± 22.7	744.4 ± 15.1	3170.32 ± 73.00	5915.10 ± 49.03	3850 ± 221[a]	2400 ± 79[a]	2050 ± 730

Notes. [a] 24 and 70 μm fluxes from 100″ radius aperture photometry. The listed c2d pipeline point-source 24 μm flux was 410 ± 200 mJy.

an average AGB contamination of less than 0.5 $\deg^{-2}$ would be expected, or fewer than one AGB star in the 2.1 $\deg^2$ area covered by IRAC and fewer than three AGB stars in the 6.5 $\deg^2$ regions covered by MIPS.

AGB stars can be identified by their low proper motions, reflecting their Galactic distances and inconsistency with membership of nearby Upper Sco. From *Hipparcos*, Upper Sco has average proper motions of $(\mu_\alpha, \mu_\delta) = (-11, -24)$ in Galactic coordinates (de Zeeuw et al. 1999; Mamajek 2008). Two of our IRAC+MIPS1 selected YSOc have inconsistent and low proper motions: YSOc 6 (IRAS 16191−1936 in OphN 3b) has proper motions of $4.7 \pm 7.2, -1.2 \pm 7.2$ mas yr^{-1} (Roeser et al. 2010) and YSOc 7 (OphN 6) has proper motions of $-2.6 \pm 5.5, 2.3 \pm 5.5$ mas yr^{-1}. Neither of these are consistent with a nearby location in Oph N, whereas the other YSOcs all show proper motions consistent with Upper Sco.

Additionally, AGB stars show a steep spectral index at long wavelengths: a criterion of $[8.0] - [24] < 2.2$ can be used to select them, though this criterion alone will not distinguish them from YSOcs (Whitney et al. 2008; Robitaille et al. 2008). Figure 9 shows several combinations of colors and magnitudes of the YSO and AGB candidates compared to those of the known AGB sample in Serpens (identified by infrared spectroscopy; Oliveira et al. 2009). It can be seen that the two IRAC-observed AGB candidates in Oph N lie in the same region in color–magnitude space as the confirmed AGB stars. YSOc 6 (IRAS 16191−1936 in OphN 3b) has $[8.0] - [24] = 1.2$ and YSOc 7 (OphN 6) has $[8.0]-[24] = 1.0$. These two sources are among the most luminous in our sample, as shown in Figure 6. In Figure 9, YSOc 9 also has the colors of an AGB candidate, but its proper motions are consistent with membership of Upper Sco ($\mu_\alpha, \mu_\delta = -3.9 \pm 4.9, -29.9 \pm 4.9$ mas yr^{-1}; Roeser et al. 2010).

In addition, two of the MIPS-selected YSOcs are likely to be background AGB stars. Sources M1 and M2 both have low proper motions inconsistent with Upper Sco: M1 ($\mu_\alpha, \mu_\delta = -4.7 \pm 4.9, -1.0 \pm 4.9$ mas yr^{-1}) and M2 ($-4.7 \pm 4.9, -1.0 \pm 4.9$ mas yr^{-1}; Roeser et al. 2010). IRAC fluxes at 8 μm are not available to apply the Whitney et al. $[8.0] - [24] < 2.2$ color criterion exactly, but applying the same principle to *WISE* fluxes these two sources have the steepest spectra of the sample between 12 and 22 μm ($[12] - [22] < 1.0$), supporting their identification as AGB stars. In the ASAS variable stars catalog, M1 is identified as a Mira variable with a magnitude variation of 1.9 mag and period 274.050380 days (ASAS 165122−1602.9; Pojmanski et al. 2005).

The four AGB candidates among the YSOcs are identified by footnotes in Tables 5 and 7 and in Figures 10–13. They are not counted in our final YSOc tally (Section 4).

3.6. 70 μm Emission and SCUBA Maps

Nine out of the ten YSOcs listed in Table 5 and two out of four of the MIPS-only YSOcs in Table 7 were observed and detected at 70 μm. Detections at 70 μm are either a sign of disk excess or a dusty envelope, as is clear from the SEDs (Figure 6). Often, these sources can also be detected in the millimeter/submillimeter (mm/submm), on the long-wavelength side of the peak of the SED. In Figure 10, we show the MIPS 70 μm maps overlaid with contours of submm emission where available. The 70 μm maps show striping artifacts remaining from the reconstruction (Evans et al. 2007). We searched the re-reduced SCUBA archive for 850 μm maps associated with the Oph N regions (Di Francesco et al. 2008) and found existing small SCUBA maps associated with parts of OphN 1 and OphN 3 (originally published in Visser et al. 2002), L234E (Kirk et al. 2005), and CB68 (Huard et al. 1999; Vallée et al. 2003; Young et al. 2006). The two YSOcs in the south of OphN 3 and in OphN 6 do not appear to have been mapped by SCUBA, and we are not aware of any other mm/submm continuum observations of these sources.

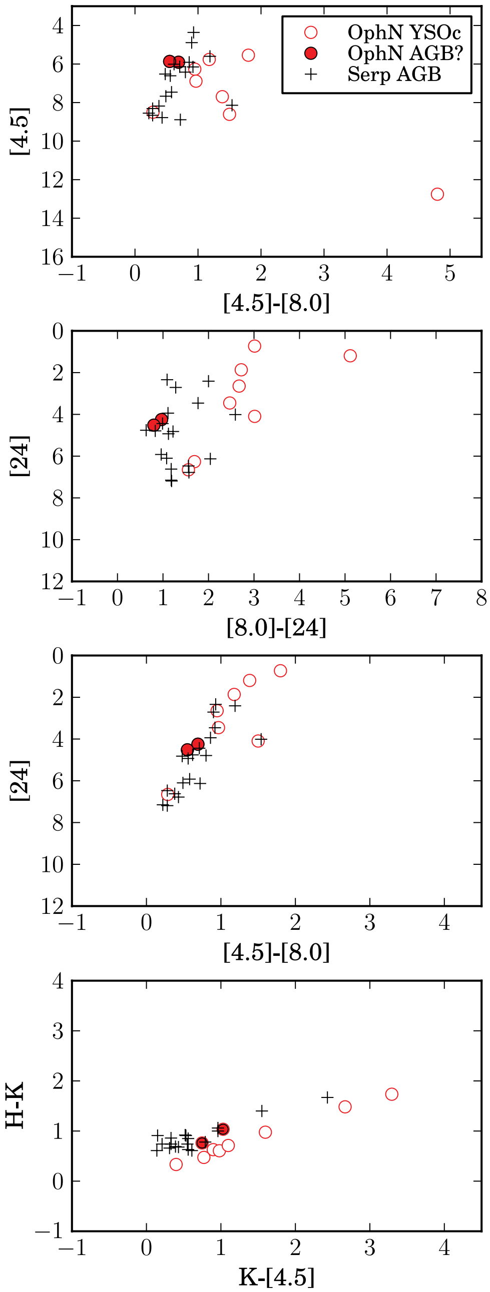

Figure 9. Color–magnitude diagrams for the IRAC-detected YSOc (open circles) comparing the AGB candidates (filled circles) with the spectroscopically identified AGB stars in Serpens (+; P. M. Harvey 2012, private communication; from Oliveira et al. 2009). The color–magnitude combinations are the same as Figure 5, though unlike that figure the galaxy interloper 6dFGS gJ164828.8−141437 is not shown. The YSOc occupying the same region of the graph as the AGB stars, but with the lowest 24 μm fluxes and bluest [4.5] − [8.0] colors, is YSOc 9.

(A color version of this figure is available in the online journal.)

Of the two Class I YSOcs, CB68 has a 70 μm detection: the OphN 1 Class I lies just off the edge of the 70 μm map. Both have been mapped and detected at 850 μm by SCUBA (Visser et al. 2002; Huard et al. 1999). The flat-spectrum source (YSOc 8 in OphN 6) is also detected at 70 μm. All but one of the Class IIs are detected: the exception is the MIPS-only Class II YSOc M4 in OphN 6. Neither the Class III source YSOc9 nor the AGB candidates YSOc7 and M1 are detected at 70 μm, as expected from the mid-infrared falloff of the SEDs (Figures 6 and 8).

3.7. *Extinction Maps*

Extinction maps provide an alternative measure of the cloud structure in Oph N. The *Spitzer* Gould Belt catalog includes a measure of the visual extinction A_V toward every source with an SED fitted by a reddened stellar photosphere (i.e., classified as a star). By convolving the extinctions at each position with a Gaussian beam, these values have been turned into extinction maps for all the area in Oph N covered by IRAC. The detailed procedure is explained in the c2d delivery document (Evans et al. 2007), but in summary, extinction maps are provided at a range of spatial resolutions, with the maximum resolution limited by the number of stars which contribute extinction measurements within each beam. As this number decreases, the uncertainties in the extinction increase. For the Gould Belt extinction maps to be accepted, a maximum of 10% of beams at any given A_V level were allowed to be undersampled, defined as containing no stars within the beam FWHM. Thus, the lowest resolution Oph N maps were sampled with a 300″ beam but the highest resolution A_V maps vary from 90″ (OphN 4 and 5) through 120″ (OphN 1, 3, and 6) to 150″ in the high-extinction OphN 2. The extinction maps are made primarily using stars with IRAC detections and at least one good 2MASS detection. In addition, a limited number of stars with no 2MASS detection but good IRAC detections are used to supplement the measurements in the higher extinction regions ($A_V > 8.5$), where the number of near-infrared detections is reduced.

Extinction maps at 150″ resolution (the highest resolution available for Oph N regions 1–6) and 120″ resolution (L234E, CB68) are plotted as black contours over the MIPS 24 μm mosaics in Figure 11. The advantage of the *Spitzer*-derived extinction maps over the optical (Dobashi et al. 2005) or near-infrared (Rowles & Froebrich 2009) is that they can probe high extinctions at relatively high resolution and so can detect compact, high column density cores. This is particularly useful in Oph N where extensive mm/submm maps are not yet available.

The mid-infrared-derived extinctions shown in Figure 11 are higher than the extinctions derived from 2MASS colors (Rowles & Froebrich 2009; Froebrich et al. 2005) by typically 2 mag and from optical star-count extinctions of Dobashi et al. (2005) by typically 3 mag. This can be seen from the contours on the extinction maps in Figure 11: the $A_V > 3$ regions from the Dobashi et al. (2005) star-count extinction maps (blue dashed contours) correspond roughly to $A_V > 4$ on the Rowles & Froebrich (2009) near-IR extinction maps (shown as red dashed contours) or $A_V > 6$ on the *Spitzer* extinction map (base level of black contours). The IRAC selection (black boxes) was based on the Dobashi et al. (2005) $A_V = 3$ contour. The reason for this difference in extinction level is not simple and requires further explanation. A significant difference between the extinction maps produced for the *Spitzer* Gould Belt survey compared to those for c2d is that no extinction offset is subtracted from the *Spitzer* Gould Belt regions. For the c2d maps, an extinction offset was calculated using off-cloud fields believed to be free of extinction from the molecular cloud. These offsets, which for the Ophiuchus cloud lying nearest to Oph N is $A_V = 1.96$, were subtracted from the on-cloud extinctions. It was believed that these corrections were for foreground, line-of sight extinction from the diffuse interstellar medium. From a detailed comparison of the mid-infrared extinction law with the models (Chapman et al. 2009) it is now thought instead that these extinction offsets are due to deviations from the assumed Weingartner & Draine (2001) $R_V = 5.5$ extinction law in the

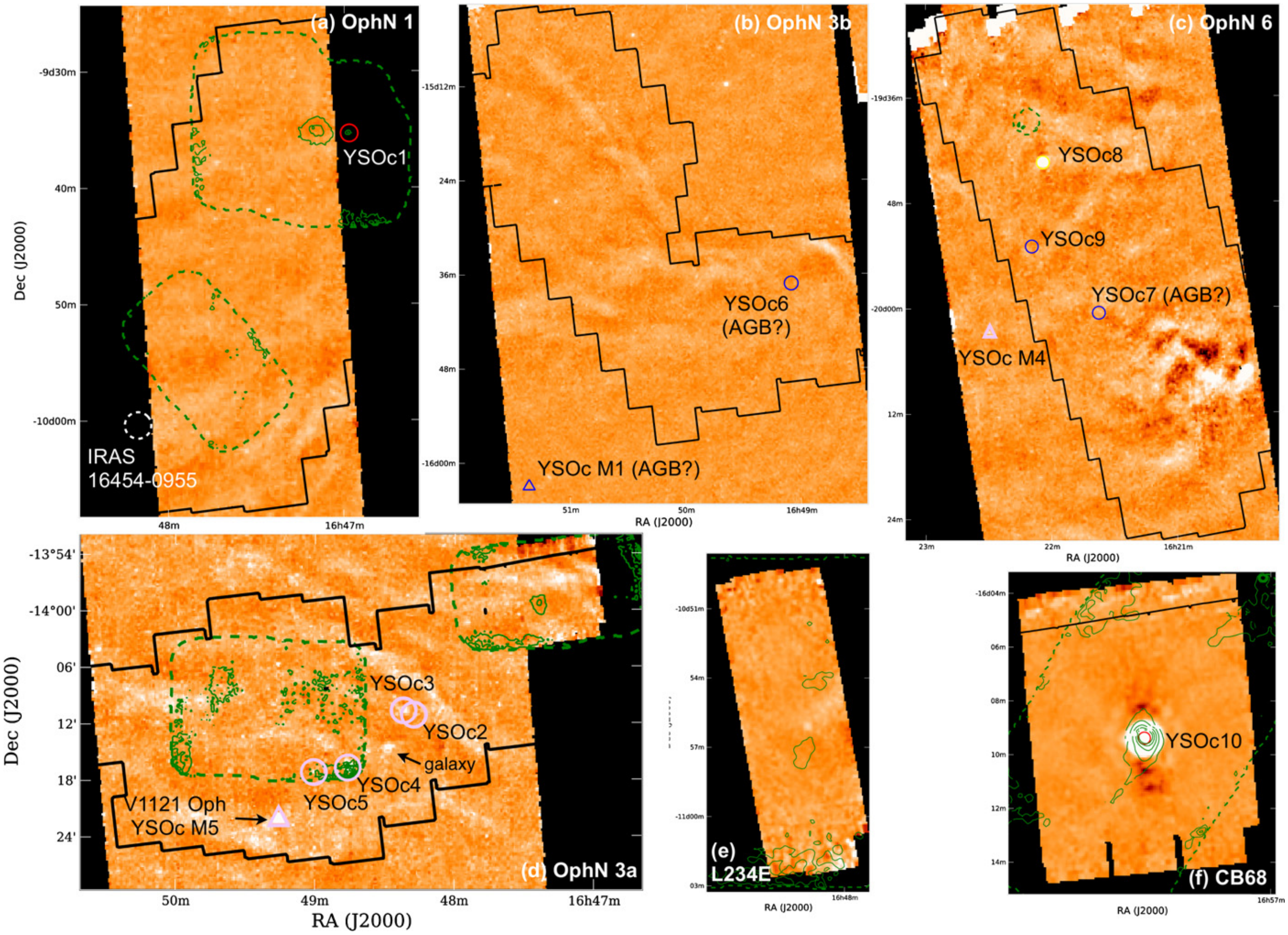

Figure 10. SCUBA 850 μm contours (green in the online version; from 100 mJy beam^{-1} in steps of 100 mJy beam^{-1}) overlaid on MIPS 70 μm maps (gray/color scale; logarithmic from −10 to 5 MJy sr^{-1}). Top to bottom: left to right: (a) OphN 1, (b) OphN 3b, (c) OphN 6, (d) OphN 3a, (e) L234E, and (f) CB68. The regions mapped by IRAC (band 1) are marked in black. Circles and triangles represent IRAC-detected and MIPS-only YSO candidates from Tables 5 and 7, respectively. YSOcs identified using IRAC and MIPS are marked with circles, and those identified using MIPS and 2MASS with triangles (in the online version, colored according to YSO class: red, Class I; yellow, flat spectrum; pink, Class II; blue, Class III). The T Tauri star V1121 Oph, the confusing galaxy gJ164828.8−141437, and the possible YSO IRAS 16454−0955 are also marked. The three regions which are starless and unobserved by SCUBA are not shown (OphN 2, 4, 5).

(A color version of this figure is available in the online journal.)

mid-infrared region of the spectrum when A_V is low. A_V was calculated assuming that the extinction law can be parameterized as $A_\lambda(R_V, \lambda)$ with $R_V = 5.5$ (Weingartner & Draine 2001; Cardelli et al. 1989). The conversion of mid-IR extinction to A_V is nonlinear with the $R_V = 5.5$ model producing reasonably reliable estimates of A_V at high extinctions ($A_V > 10$) but overestimates at low extinctions ($A_V < 10$) by a factor which varies with A_V and cloud. This is the cause of the apparent extinction in the off-cloud fields, and the difference of $A_V = 2$–3 from the extinction maps derived at shorter wavelengths.

The high extinction regions are small and fragmented, typically less than a parsec in size. The masses in each region above extinction thresholds of $A_V = 6$, 10, and 20, derived from these maps, are given in Table 9. Approximately 100 solar masses of gas lie at $A_V > 10$ in Oph N, split between 12 clumps (Figure 11). This is about 1/30 of the mass in Ophiuchus though similar to Lupus I or IV (Heiderman et al. 2010). Each individual clump only has a mass reservoir of order 10 $M_\odot$, sufficient to form a few low-mass stars. Several Oph N regions show cores of $A_V \geqslant 20$ in the 150″ resolution *Spitzer*-derived extinction maps: there is one in OphN 1, two in OphN 2, and three in OphN 3 (Figure 11). The OphN 1 and CB68 cores contain the two Class I YSOs OphN YSO1 and 10, respectively, but the other extinction peaks are currently starless. Class II and III YSOs lie on the edges of the extinction regions in OphN 3a, 3b, and OphN 6.

Table 9
Core Masses above Extinction Thresholds

Region	$M(A_V > 6)$[a] ($M_\odot$)	$M(A_V > 10)$ ($M_\odot$)	$M(A_V > 20)$ ($M_\odot$)
OphN 1	30	10	1
OphN 2	51	17	2
OphN 3	149	52	7
OphN 4	9	0	0
OphN 5	6	0	0
OphN 6	40	5	0
CB68	1	0	0
L234E	8	1	0
	294	85	10

Notes. [a] The $A_V = 6$ masses are lower limits as these regions extend beyond the limits of the map. See Figure 11.

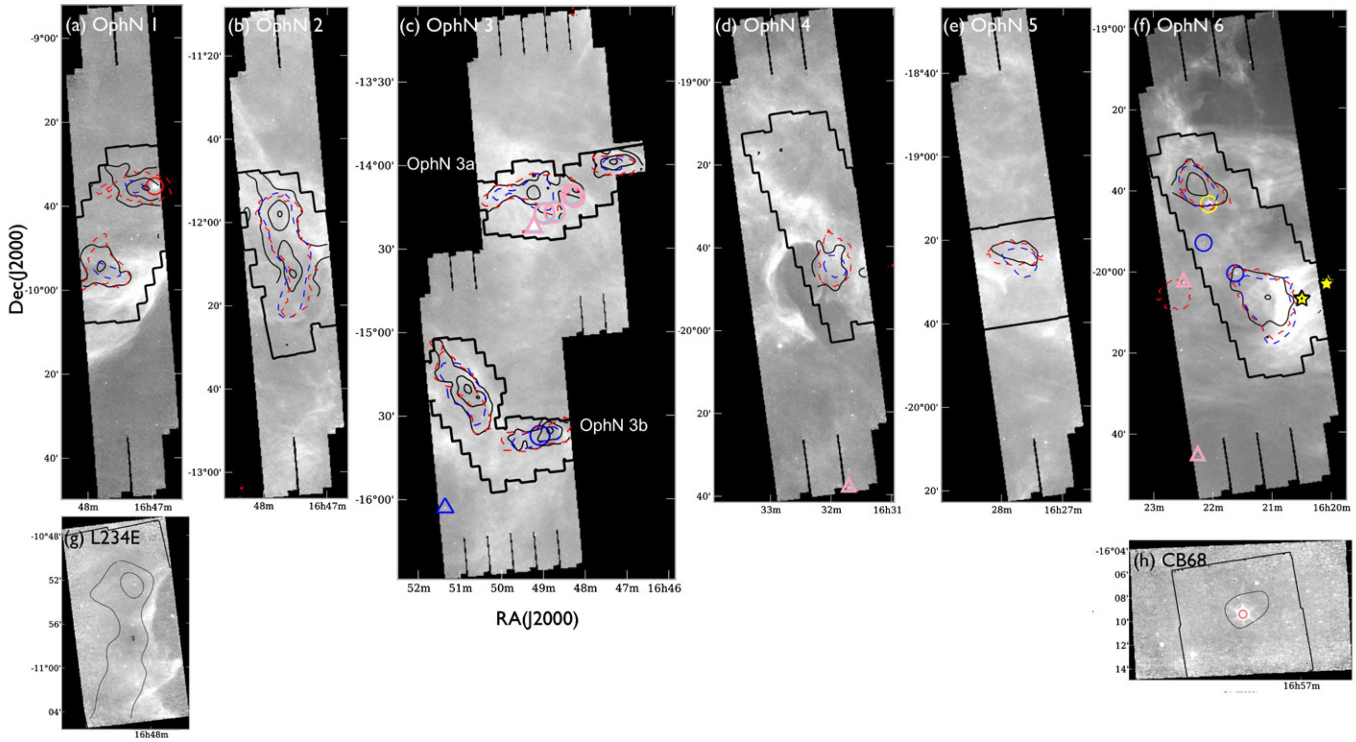

Figure 11. MIPS 24 μm maps (color scale) overlaid with *Spitzer*-derived extinction contours at $A_V = [6, 10, 20]$ (black) for the areas observed by IRAC. Top left to bottom right: (a–f) OphN 1, 2, 3, 4, 5, and 6, (g) L234E, and (h) CB68. For comparison, the $A_V = 3$ level from optical star counts (Dobashi et al. 2005) and $A_V = 4$ from near-infrared colors (Rowles & Froebrich 2009) are plotted with dashed contours (blue and red respectively in the online version). Sources are marked as in Figure 10.

(A color version of this figure is available in the online journal.)

3.8. 160 μm and IRAS Maps

Emission at wavelengths of 100 μm and longer is dominated by cold dust and extended cloud structure. In addition to the MIPS 160 μm data, we also obtained *IRAS* 100 μm images that were resolution enhanced using the HIRES algorithm.[16] Image coordinates were additionally precessed from B1950 to J2000 coordinates using the Goddard IDL astron library. The algorithm improves the spatial resolution from the native *IRAS* ($3'.8 \times 5'.4$) to $2'$ at 100 μm wavelength (Cao et al. 1997). The MIPS 160 μm data have a factor five better spatial resolution of $40''$. The HIRES processing provides sharper and more clearly defined filaments and other extended structure. Point sources are, however, surrounded by a ringing artifact. Since our focus is on the extended structure, the point sources are removed from the 100 μm image using median pixel replacement.

The *Spitzer* 160 μm and *IRAS* 100 μm maps are shown side-by-side in Figure 12. The *IRAS* 100 μm maps have broader spatial coverage and show the continuous filamentary structure linking the OphN 1–3 clouds. The OphN 4 and 5 clouds are also linked by 100 μm emission which takes the form of several cavities or bubbles. Although there are ionizing stars in the region, these lie to the north (the B2V star χ Oph at $l, b = 357.93, +20.68$ and, in the past Myr, ζ Oph; see Figure 1 of this paper and Figure 5 of Nozawa et al. 1991) whereas the openings of the bubbles lie to the south. The bubbles themselves contain no ionizing stars to produce H II regions. A possibility is that they could be fluid instabilities at a hot gas/cold cloud interface where the flow from the Upper Sco H I bubble has broken out (see discussion in de Geus 1992).

The extended emission exhibits structure that is very similar at both 100 and 160 μm, apart from resolution effects. This similarity indicates that the two wavelengths are mostly tracing the same dust component. To determine the dust temperature and derive physical parameters we follow the technique presented in Terebey et al. (2009) and briefly described here. For thermal dust emission the intensity I_ν at frequency ν is given by $I_\nu = \tau_\nu B_\nu(T)$, appropriate for low optical depth and where $B_\nu(T)$ is the Planck function and τ_ν the optical depth. The wavelength dependence of the optical depth is given by the usual $\tau_\nu \sim \nu^\beta$ where $\beta = 1.5$–2 at long wavelengths. If, for example, the dust temperature is constant across the image then the Planck term $B_\nu(T)$ is constant. The result is that the 160 and 100 μm images will look identical, apart from resolution effects, while the structure in the images will linearly trace the optical depth i.e., column density. Also, a plot of I100 versus I160 intensity values for each image pixel will exhibit a linear trend whose slope is related to the dust temperature. In practice, the assumption of constant dust temperature works well over scales of 1°–2°.

Table 10 shows the I100 versus I160 slope and corresponding dust temperature for each of the seven OphN regions separately. There is a small but real trend in dust temperature across the region. The coldest dust temperatures are found in OphN 1 (15.6 K) and OphN 3S (15.9 K) located on the eastern side, while the warmest temperatures are in OphN 5 (17.0 K) and OphN 6 (16.8 K) located on the western side, nearest the OB association as seen in the projection. The higher dust temperatures on the western side support the idea that the OB stars enhance the local interstellar radiation field. In comparison, the Taurus star-forming region has colder 14.2 K dust (Terebey et al. 2009;

---

[16] http://irsa.ipac.caltech.edu/IRASdocs/hires_over.html

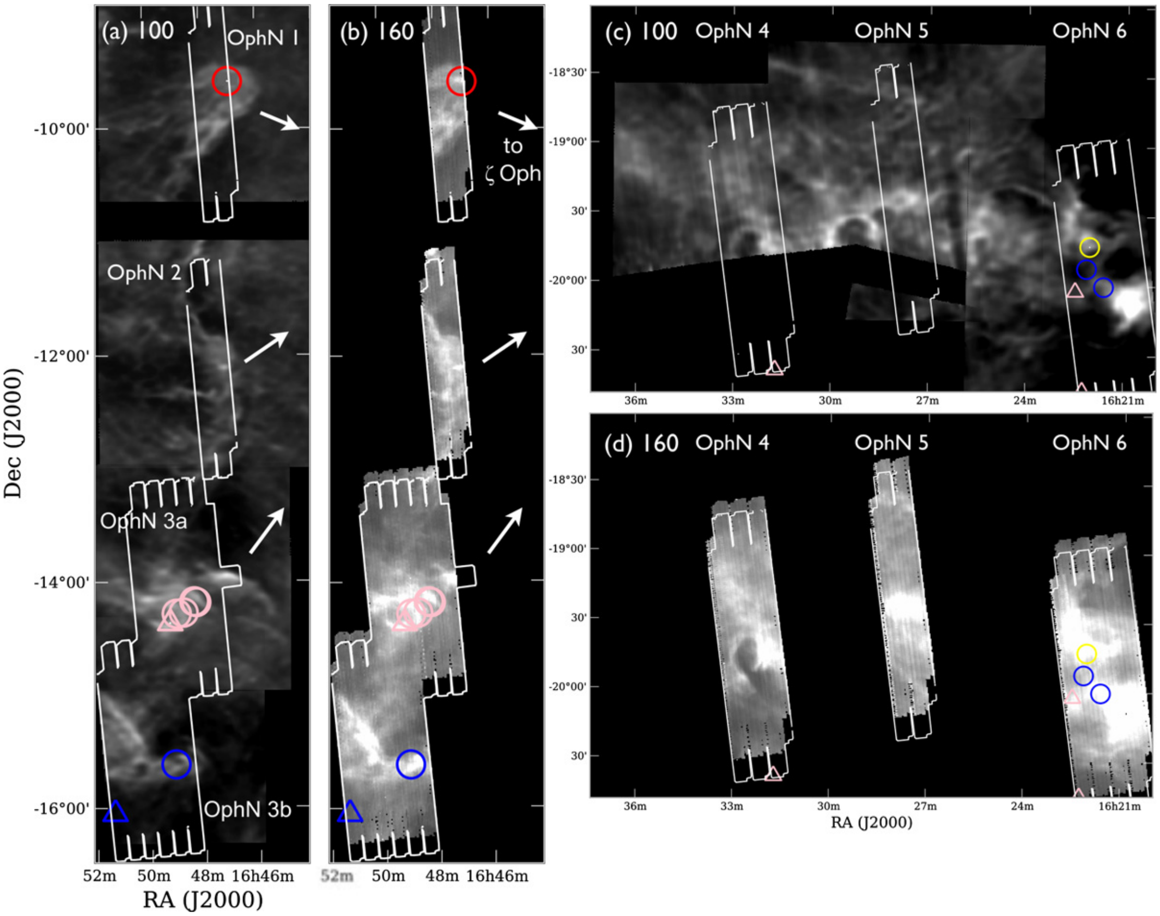

Figure 12. *Spitzer* 160 μm emission and *IRAS* HIRES-processed 100 μm emission. Left to right, top to bottom: (a) *IRAS* 100 μm image of OphN 1, 2, and 3, with arrows indicating the approximate direction of ζ Oph; (b) *Spitzer* 160 μm image of OphN 1, 2, and 3; (c) *IRAS* 100 μm image of OphN 4, 5, and 6; (d) *Spitzer* 160 μm image of OphN 4, 5, and 6. Gray scales are a square-root stretch from -10 to 50 MJy sr^{-1} (*IRAS* 100 μm) and from 10 to 150 MJy sr^{-1} (*Spitzer* 160 μm). Sources are marked as in Figure 10.

(A color version of this figure is available in the online journal.)

Table 10

100/160 μm Spectral Slope and Average Dust Temperatures

Region	Slope[a]	T_d/K[b]/$\beta = 2.0$
OphN 1	0.35	15.6
OphN 2	0.39	16.1
OphN 3S	0.37	15.9
OphN 3N	0.40	16.3
OphN 4	0.39	16.1
OphN 5	0.45	17.0
OphN 6	0.44	16.8

Notes.

[a] Uncertainty in slope is ±0.002. Estimated systematic uncertainty of 10% leads to ±0.4 K absolute temperature uncertainty.

[b] Color-corrected dust temperature for $\beta = 2.0$. Changing from $\beta = 2.0$ to $\beta = 1.7$ (appropriate for Ossenkopf & Henning 1994 model OH5 dust opacity) leads to dust temperatures that are 0.8 K systematically higher.

Flagey et al. 2009), consistent with the lack of luminous heating sources in Taurus.

All but one of the Oph N regions show evidence for cold clumps in the excess map (Figure 13). In OphN 1, these are associated with L260 SMM1 and 2. The 160 μm excess peaks at the Class 1 protostar OphN YSOc1 which is indicative of a cold disk or envelope. By contrast, there is no enhancement at the positions of the Class II and III sources in OphN 3 although the clouds in the south of the region appear cold. The effects of UV heating, presumably from ζ Oph, can be seen along the northern edges of these clouds as bright 100 μm features and negative values in the 160 μm excess maps. OphN 4 exhibits one of the series of bright shells or loops best seen in the 100 μm maps. The moderate extinction clump on the edge of this cavity is warm. There is also little cold dust in OphN 5. By contrast, OphN 6 shows two cold clumps and cold dust associated with the flat-spectrum source OphN YSO8 (L1719B).

4. DISCUSSION

The *Spitzer* data advance our knowledge of Oph N with an improved list of candidate YSOs, higher-resolution extinction maps, and dust temperature estimates. In this discussion, we apply this information to revisit the YSO population, the current star formation rate/efficiency, and the evidence for triggering and other effects of the neighboring Upper Sco OB association on the region.

4.1. Star Formation Count and Efficiency

How many stars are currently forming in the Oph N clouds? In the areas covered by both *Spitzer* IRAC+MIPS, 10 YSOcs are identified. In the areas with no or limited IRAC coverage, MIPS+2MASS colors add a further five. A further Class I source, RNO91, is detected in L43 (Chen et al. 2009), bringing the total to 16. This count almost doubles the nine sources

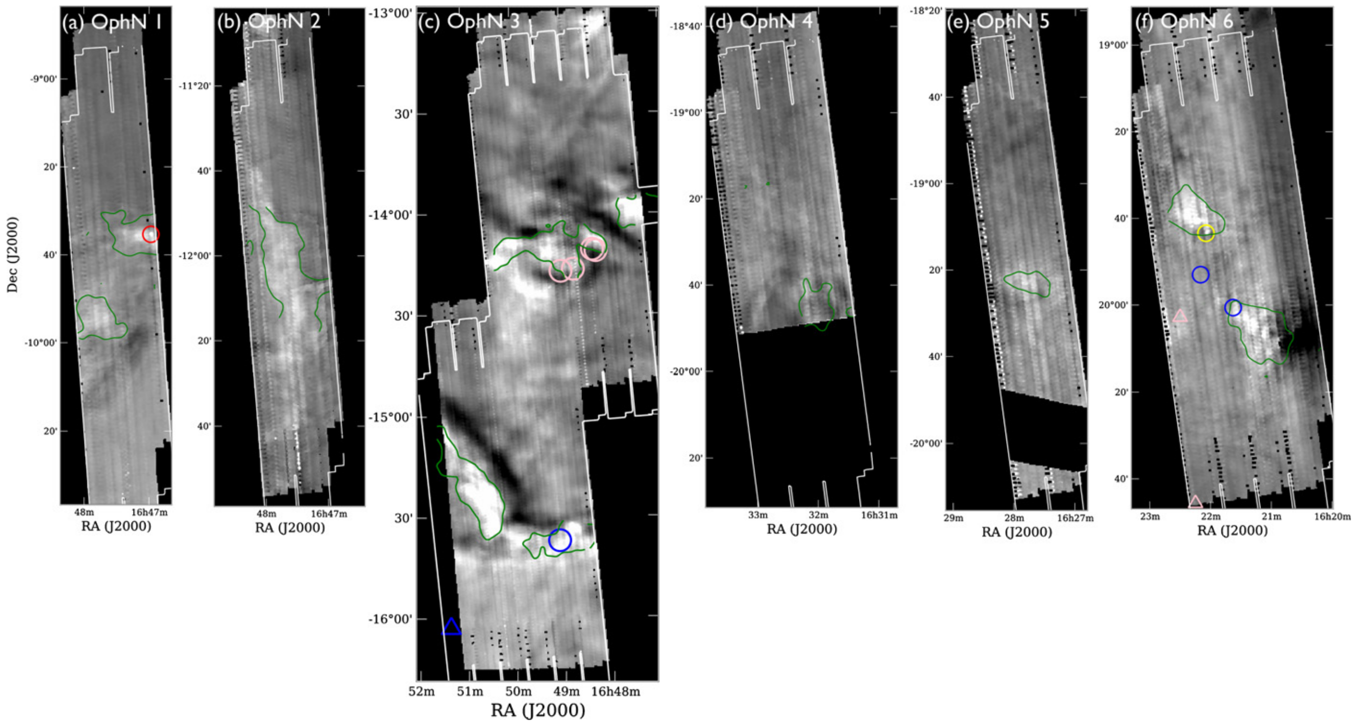

Figure 13. Excess 160 μm over 100 μm emission (gray scale, linear from −50 to 50 mJy sr^{-1}) overlaid with *Spitzer* $A_V = 6$ contour (green in the online version, shown in the IRAC regions only). Left to right: (a–f) regions OphN 1, 2, 3, 4, 5, and 6. CB68 and L234E have no 160 μm map and are not shown. Sources are marked as in Figure 10.

(A color version of this figure is available in the online journal.)

known from *IRAS* (Carballo et al. 1992). However, four of these candidates (including two of the *IRAS* detections) are probable AGB stars based on their colors and proper motions (Section 3.5). Excluding the AGB stars, the total number of *Spitzer*-identified YSOcs in Oph N is 12.

However, the area of Oph N molecular clouds surveyed by *Spitzer* is limited and it is possible that additional YSOs lie outside the mapped region. Based on the low extinction these are likely to be Class II/III sources. We can estimate the number of YSOcs missed by *Spitzer* by considering the number of *IRAS* detections within and outside the *Spitzer* regions. *IRAS* covers the whole of the Oph N region but is less sensitive than *Spitzer*: of the 12 *Spitzer* YSOcs (including RNO91 in L43, excluding probable AGN), only 7 have *IRAS* identifications.

A wider area search for YSOs in Oph N was made by Carballo et al. (1992) based on *IRAS* colors. Excluding the Ophiuchus and Lupus clouds, they identify six *IRAS* sources in the Oph N region as definite YSOs, five of which are cross-identified by *Spitzer* and one of which lies outside the *Spitzer* regions (T Tauri stars V1003 Oph or RNO90 near L43). A further *Spitzer* YSOc (Oph N YSOc3 or IRAS 16455−1405) is among a further 10 *IRAS* sources ambiguously classified by Carballo et al. (1992) as either YSOs, galaxies, or EGOs and one further *Spitzer* candidate, YSOc 4, has an *IRAS* identification not listed by Carballo et al. (1992; though included by Nozawa et al. 1991), bringing the total number of *Spitzer* sources detected by *IRAS* to seven. Hence, with the count of *IRAS* YSOs outside the *Spitzer* regions numbering one, our *Spitzer* survey encompasses 7/8 or 88% of the *IRAS*-identified YSOs in the region.

In addition, there are four ambiguous (as classified by Carballo et al. 1992) *IRAS* detections outside the *Spitzer* regions which have associated extinction $A_V \geqslant 1$. If these also turn out to be YSOs (e.g., IRAS 16534−1557 or IRAS 16439−0945; see Appendices A.1 and A.8) the completeness decreases further to 7/12 or 58%. None of these are associated with MIPS-only sources. Assuming these statistics hold for all 12 of the *Spitzer* identified YSOcs, and not only the 7 detected by *IRAS*, the true number of YSOs in Oph N (north of the Ophiuchus L1688 and L1689 clouds) is likely to lie between 14 and 21.

The star formation surface density in Oph N has been addressed recently by Heiderman et al. (2010; under the region name "Scorpius"), who find a star formation rate per unit area $\Sigma_{\rm SFR} = 0.343 \pm 0.20\, M_\odot\, {\rm yr}^{-1}\, {\rm kpc}^{-2}$ based on the ten *Spitzer* IRAC+MIPS identifications reported here and comparing with an $A_V > 2$ area of $7.29\, {\rm pc}^2$. This is among the lowest in Gould Belt clouds (mean $\Sigma_{\rm SFR} = 1.2 \pm 0.2\, M_\odot\, {\rm yr}^{-1}\, {\rm kpc}^{-2}$), comparable to Lupus I, Auriga N, and IC5146 E/NW but only 15% of that in Ophiuchus ($2.45 \pm 1.6\, M_\odot\, {\rm yr}^{-1}\, {\rm kpc}^{-2}$). The inclusion of RNO91 and the three MIPS+*WISE* identifications, but the exclusion of two AGB stars, increases the rate to $\Sigma_{\rm SFR} = 0.412 \pm 0.25\, M_\odot\, {\rm yr}^{-1}\, {\rm kpc}^{-2}$.

An estimate of the instantaneous star formation efficiency (SFE) $M_*/(M_* + M_{\rm gas})$ can be made comparing the total 12 YSOcs to the total mass in the Oph N clouds, which is 3000 $M_\odot$ calculated for $A_V > 1$ in the Dobashi et al. (2005) map, consistent with 4400 $M_\odot$ from ^{13}CO (Nozawa et al. 1991). Assuming 12 YSOcs with an average stellar mass of 0.5 $M_\odot$ (following Evans et al. 2009) gives an overall SFE of 0.20%. Taking into account the survey incompleteness gives an upper limit of 0.34%. These efficiencies are consistent with the 0.3% upper limit given by Nozawa et al. (1991; we assume half their average stellar mass and a slightly different star count, 12 rather than 13).

Nozawa et al. (1991) suggest two reasons for the low SFE: the cloud is clumpy and fragmented, with only a small fraction of the mass in high column density cores; and the UV radiation estimated from the nearby OB stars is a factor of two higher than the standard Habing field, leading to high cloud ionization and magnetic support. These estimates of the instantaneous SFE do not take into account the earlier formation of the main-sequence stars in Upper Sco. However, we confirm the result of Nozawa et al. (1991) that the current star formation efficiency in the cloud complex is very low.

4.2. Comparison with Ophiuchus

This low star formation efficiency is completely unlike the nearby Ophiuchus L1688 cloud, which is forming a dense embedded cluster (e.g., Padgett et al. 2008). Measured in low-excitation ^{13}CO 1–0, the Oph N and Ophiuchus cloud masses are similar: 4000 $M_\odot$ compared to 3050 $M_\odot$ (L1688, L1689, and L1712-1729 filament; Loren 1989; Nozawa et al. 1991). The main difference between the cloud complexes is the mass in dense gas. From the Rowles & Froebrich (2009) 2MASS-based extinction maps, calculated identically for the two clouds, we calculate that Oph N has 25% the mass of Oph above $A_V = 3$ (680 $M_\odot$ in Oph N), dropping to 4% of the mass at $A_V > 5$ and less than 0.5% for $A_V = 10$. Tachihara et al. (2000b) found that traced in C^{18}O 1–0, the cores in L1688 are 10 times denser than the others in the region, and 32% of the cloud mass is traced by C^{18}O compared to 8% in the Oph N clouds, indicating substantial optical depths in the ^{13}CO (Tachihara et al. 2000b). As studies extend beyond the more obvious star-forming regions, many molecular clouds are seen to fit this pattern of extended low column density material with a few low-mass cores, but the Oph N clouds are particularly inefficient: the Lupus molecular clouds—also on the edge of Sco–Cen association—have a star formation efficiency of a few percent (Tachihara et al. 1996; Merín et al. 2008); Taurus is also less extreme than Oph N with a star formation efficiency of 1%–2% (Mizuno et al. 1995). Maddalena's cloud (G216-2.5) is a more extreme example with a mass of more than a million $M_\odot$ only a few dozen YSOs (Megeath et al. 2009).

4.3. Prestellar Cores

There is no evidence that star formation is coming to an end in the Oph N region. The YSOcs cover the full range of evolutionary classes (three Class 0/1; one flat spectrum; seven Class II; one Class III), and there are also several dense starless cores in the region, including submm cores in L234E, L255 SMM2 in OphN 1, and L158 in OphN 3a. Star formation is clearly still ongoing in Oph N, though at a low rate.

A statistical estimate of the starless core lifetime can be made from the high extinction cores. Considering $A_V > 10$ cores, the ratio of starless to protostellar cores is 12:3 (from Figure 11, including CB68, L234E, and one starless and one protostellar core in L43). If the starless cores are prestellar cores, then this ratio suggests that their lifetime is a factor of four longer than the protostellar lifetime of 0.54 Myr (Evans et al. 2009; Hatchell et al. 2007) or ∼2 Myr. This is consistent with expectations for lifetime versus volume density (Ward-Thompson et al. 2007, Figure 2) given a typical core density of 7×10^3 cm^{-3} (Nozawa et al. 1991, from C^{18}O). This is further support for the idea that the restrictive step in Oph N is the formation of dense cores from low density material.

4.4. Influence of Upper Sco OB Association

With a known age gradient through the OB associations from Upper Centaurus-Lupus to Upper Scorpius to Ophiuchus, Oph N would seem an ideal region in which to look for the effect of triggering on star formation. But while there is ample evidence for the dynamical and radiative influence of Upper Sco on the region, the low star formation efficiency and normal fraction of starless cores do not suggest that star formation has been promoted, even in the clouds most strongly affected by the nearby OB association.

An expanding H i shell surrounds Upper Sco, created by the stellar winds and possibly the supernova explosion of the binary partner of runaway ζ Oph, impacting on the Ophiuchus and Oph N clouds from the west (de Geus 1992). According to de Geus (1992), the expansion of the shell in this region is halted by the Ophiuchus and OphN 6 dense cores, with molecular gas swept from the main clump to produce OphN 4 and 5 and the elongated Ophiuchus filaments to the south. A relatively recent origin is consistent with the absence of star formation in OphN 4 and 5 but could be tested by chemical comparison with OphN 6. Both OphN 5 and OphN 6 have elevated temperatures (Section 3.8). The bubbles seen in the 100 μm maps of OphN 4 and 5 also suggest dynamic disruption of these clouds. A similar though less extreme lack of star formation is seen in Oph L1689 compared to L1688, where the effects of the O-star σ Sco are strongest (Nutter et al. 2006). The OphN 6 and Ophiuchus clouds are at similar distances to Upper Sco, so the physical input from winds and radiation must have been similar in each region. The difference in the star formation points to differences in the initial conditions, with the gas in Oph L1688 sufficiently gravitationally bound to survive—and even benefit from—the onslaught from Upper Sco, whereas the gas in OphN 6 had too low a density to counter the feedback forces. Timescales are too short for the formation of the Class II and III sources in the L43, OphN 3, and OphN 6 clouds to have been initiated by this most recent shock, which has an upper limit on its expansion timescale of 2.5 Myr and may not even yet have reached these clouds (Tachihara et al. 1996). There is also no clear sequence in protostellar ages from the front to the back of the filament which would suggest that the star formation has been triggered by the interactions with Upper Sco OB association.

The UV field from the runaway O-star ζ Oph forming the S27 H ii region is possibly an earlier influence on the northern Oph N clouds and L43 (Tachihara et al. 2000a). The dense gas in OphN 1 and 2 mainly lies along the west side of the filament and the clouds are also heated along this side (Section 3.8). The 100 μm maps show bright rims to the west and north in the direction of ζ Oph and sharp boundaries in the dust distribution. ζ Oph (09.5) originates in Upper Sco and has since tracked from southwest to northeast across the northern Oph N region on timescales of a few times 10^5 years (see Tachihara et al. 2000a, Figure 5). The radiation has impacted OphN 1 and L43 and may have contributed to the compression of the cores hosting Class 0/I sources in L43 and L260. The 2 Myr old T Tauri stars in OphN 3 and RNO90 near L43 predate the impact of the H ii region. A study of the energetics suggests that UV photodissociation from ζ Oph is currently accelerating gas from the remaining dense cores toward the east (Tachihara et al. 2000a). This is also suggested by the bright rims and cometary nature of OphN 1–3 as seen in the 100 μm *IRAS* map (Figure 12). It seems likely that the small star-forming molecular cores in Oph N are the surviving remnants of the giant molecular cloud which produced Upper Sco and are now slowly being ablated by the massive stars.

5. CONCLUSIONS

We have surveyed the high extinction regions ($A_V > 3$) of the Oph N molecular cloud complex in the mid-infrared with *Spitzer* IRAC and MIPS.

There is little active star formation in Oph N. Twelve YSOcs are identified in total. Eight of these are identified from their IRAC–MIPS colors. An additional Class I protostar exists in the L43 cloud in the center of this region (Chen et al. 2009). Three further YSOcs are found based on red $[K - 24]$ colors. Four sources initially selected as YSOcs were rejected as AGB stars and one as a galaxy. Of the 12 remaining YSOcs, 3 are Class I, 1 flat spectrum, 7 Class II, and 1 Class III. All except one Class III and two Class II sources were previously known. The region as a whole has a low star formation efficiency of $<0.34\%$.

The high extinction regions in Oph N are fragmented into 12 small (∼0.2 pc), scattered and low-mass (∼10 $M_\odot$ or less) cores, of the kind which might form one or two low-mass stars. Three of these (OphN 1, CB68, and L43) currently contain Class I sources. The remainder are starless.

The interstellar medium in this region is influenced by the Upper Sco subgroup of the Sco–Cen OB association. There is evidence for dynamical interaction in the OphN 4 and OphN 5 bubbles, elevated temperatures in OphN 5 and 6, and irradiated cloud edges throughout the region. The bulk of the gas mass is at low column density with only a few low-mass cores surviving to form a few YSOs. This is very different from the situation in nearby Ophiuchus L1688, which contains hundreds of YSOs (Padgett et al. 2008), but similar to the Lupus clouds (Tachihara et al. 1996; Merín et al. 2008). As the impact of radiation and winds from Upper Sco must have been similar in both regions, the initial conditions must have been very different. Whereas the main Ophiuchus complex contained hundreds of solar masses of dense gas, Oph N only contained a few low-mass high-density cores. It seems likely that the small star-forming molecular cores in Oph N are the surviving remnants of the giant molecular cloud which produced Upper Sco and are now slowly being ablated by the massive stars. The low star formation rate is due to the lack of dense cores.

We thank the anonymous referee for constructive suggestions. S.T. thanks Deborah Padgett for help with the *WISE* data. J.H. acknowledges support from the STFC Advanced Fellowship program. E.E.M. acknowledges support from the NSF award AST-1008908. This research has made use of the SIMBAD database, operated at CDS, Strasbourg, France; the NASA/IPAC Infrared Science Archive, which is operated by the Jet Propulsion Laboratory, California Institute of Technology, under contract with the National Aeronautics and Space Administration; and data products from the Wide-field Infrared Survey Explorer, which is a joint project of the University of California, Los Angeles; and the Jet Propulsion Laboratory/California Institute of Technology, funded by the National Aeronautics and Space Administration.

APPENDIX

COMMENTS ON INDIVIDUAL REGIONS

A.1. OphN 1

The two extinction peaks in OphN 1 lie in Lynds opacity class 6 cloud L260 (Figure 11). The YSOc and starless core are both in the more massive northern extinction region (9 $M_\odot$ above an extinction limit of $A_V > 10$, compared to a $C^{18}O$ mass of 11.4 $M_\odot$; Nozawa et al. 1991). The southern extinction peak shows no evidence for star formation or dense cores and little high-extinction gas (1 $M_\odot$ above $A_V = 10$), indicating that the $C^{18}O$ mass of 17.9 $M_\odot$ mainly lies at lower extinctions.

The Class I source YSOc1 is identified with IRAS 16442−0930/IRAS 16449−1001 and lies close to the peak of the northern core ($C^{18}O$ core u2; Tachihara et al. 2000b). This YSOc was first identified as such from the *IRAS* catalog by Carballo et al. (1992). The source is detected but unresolved in 1.3 mm continuum with a mass $<0.05\ M_\odot$ and at 850 μm by SCUBA with a peak flux less than 72 mJy beam^{-1} (L260 SMM1; Visser et al. 2002, see our Figure 10), consistent with the mm/submm emission largely originating from a disk. There is an associated ^{12}CO outflow (Bontemps et al. 1996; Visser et al. 2002) and an H_2O maser (Han et al. 1998). The *IRAS* spectrum of this source was studied in detail by Parker (1991), who concluded from a shoulder in the short-wavelength emission at 1.5–2 μm that it was a Class II YSO obscured by an extended dark cloud, but we see no evidence for this shoulder in the 2MASS fluxes.

The submm emission and the extinction in this region peak toward a second core 3′ to the east (Visser et al. 2002; L255 SMM2). No source is detected by *Spitzer* even at 70 μm (Figure 10), confirming this as a starless core.

A second *IRAS* source IRAS 16454−0955 with ambiguous colors typical of a YSO or EGO lies in the southeast of the IRAC region unobserved by MIPS (Carballo et al. 1992; marked in Figure 10). A search through the positional matches within 10″ in the *Spitzer* catalog found no reddened or rising spectra. Better waveband coverage is needed to pinpoint the source of the infrared emission detected by *IRAS*. Another ambiguous *IRAS* YSO or galaxy from Carballo et al. (1992), IRAS 16439−0945, lies to the west on the edge of the OphN 1 $A_V \sim 2$ region, but off the IRAC and MIPS maps.

A.2. L234E

South of OphN 1, L234 (Lynds opacity class 3) contains no YSOcs. The area mapped by *Spitzer* has a mass of only 1 $M_\odot$ above $A_V > 10$, though it is coincident with Tachihara et al.'s (2000b) core t ($C^{18}O$ mass 12.9 $M_\odot$). The SCUBA map shows weak 850 μm emission peaking at 130 mJy beam^{-1} (Kirk et al. 2005). The faint 70 μm source seen an arcminute to the north in Figure 10, at $16^h48^m06\overset{s}{.}6$–10°56′06″, is classified by the c2d pipeline as a galaxy.

A.3. OphN 2

This region in L204 continues the filament of bright-rimmed clouds and contains two extinction peaks over $A_V = 10$ (8 and 10 $M_\odot$ respectively), several $C^{18}O$ cores (Tachihara et al. 2000b; s1–5) with masses from 5 to 33 $M_\odot$, but no YSOcs. No submm maps exist of this region. It is a good candidate for future star formation.

A.4. OphN 3

Five Class II and III protostars are identified in the OphN 3 IRAC fields, four in the north and one in the south field. The northern sources are associated with Lynds opacity class 6 cloud L162 but are not coincident with the extinction peaks: they lie on the edge of the $A_V = 3$ region heated by ζ Oph (see Figure 11). One of the northern sources, OphN YSOc3, is associated with IRAS 16455−1405, already identified as a

YSO or (ambiguously) an EGO by Carballo et al. (1992). This star is in fact a binary with 1″ separation (Reipurth 44; Reipurth & Zinnecker 1993) and possibly even a triple system (Koresko 2002). Another potential binary is OphN YSOc2, which lies 9″ from the extended red variable T Tauri star V* V2507 Oph; both have similar proper motions consistent with the idea that these two stars form binary Reipurth 43 (Reipurth & Zinnecker 1993).

The classical T Tauri star V* V1121 Oph (IRAS 16464−1464) lies 10 arcmin to the southeast of the other northern OphN 3 YSOcs at $16^{\rm h}49^{\rm m}15^{\rm s}.3{-}14^{\circ}22'08''.6$ (André & Montmerle 1994; see our Figure 10). It is detected by IRAC bands 1 and 3 but lies outside the field of IRAC 2 and 4 and the YSOc identification comes from the $K_S - [24]$ selection (Table 7). At 24 and 70 μm it is bright but extended and confused with cirrus, and the catalog fluxes are bandfilled (see Figures 10 and 11). V1121 Oph is classified as a Class II source (André & Montmerle 1994) and, like the other Class II YSOcs 4 and 5 in OphN 3, it is bright at 70 μm (Figure 10).

The Visser et al. (2002) SCUBA 850 μm map of the L158 and L162 regions is overlaid on the 24 μm map in Figure 10. YSOc4 (Class II) is detected as a compact 850 μm source L162 SMM1 which Visser et al. (2002) identify with IRAS 16459−1411. This is a well-studied T Tauri star with a disk (André & Montmerle 1994; Andrews et al. 2009). YSOc5 is not detected by SCUBA at a level of 100 mJy beam^{-1}. Neither YSOc2 nor YSOc3 lie within the SCUBA maps. The MIPS-only Class III source M1 which lies in the southeast of the 70 μm map in Figure 11 is identified as IRAS 16484−1557. The starless core in L158 detected by SCUBA (Visser et al. 2002) remains infrared dark even at 70 μm, confirming this source as starless. The nearby *IRAS* sources IRAS 16445−1352, IRAS 16442−1351, and IRAS 16439−1353 appear to be cirrus. The L158 core lies in the most massive of the three northern extinction peaks, which have $A_V > 3$ masses of 5, 1, and 13 $M_\odot$, measuring from east to west.

The galaxy 6dFGS gJ164828.8−141437 confusingly lies among the northern OphN 3 YSOcs and was initially identified by the color–color YSOc selection procedure but rejected when examined by eye as being elliptical. It appears in the 2MASS-MIPS color–magnitude diagram (Figure 7) marked as a YSOc but clustered with the galaxies at $K_S \sim 14$. Its location within 20′ of the other YSOcs in the north of OphN 3 is particularly confusing (see Figure 10).

In the southern region we identify OphN YSOc5, classified Class III, with IRAS 16462−1532. This source is associated with the westernmost of the two extinction peaks, mass 13 $M_\odot$ ($A_V > 10$; see Figure 11). The southeastern extinction core is more massive, at 21 $M_\odot$, and a likely site for future star formation. There are no submm maps of this region to determine if it contains any dense cores. The Lynds opacity 4 and 5 dark clouds L137 and L141 lie to the north of this region, but are not associated with any YSOcs.

A.5. OphN 4

The OphN 4 field is associated with L1757, which shows no extinction above $A_V = 10$, consistent with its detection in ^{13}CO (Nozawa et al. 1991, cloud C) but not C^{18}O (Tachihara et al. 2000b). There is a bright-rimmed globule in the 24 μm map but no YSOcs. Ambiguous YSO/EGO IRAS 16355−1807 is located at the northern end of the extinction filament 2° east of OphN 4, at an optical extinction of $A_V \simeq 1$ (Carballo et al. 1992).

Table 11

Parallaxes and Proper Motions for Early-type Stars in OphN 6

HIP	Spectral Type	Parallax (mas)	mu_α (arcsec yr^{-1})	μ_δ (arcsec yr^{-1})
80019	B9[a]	5.17 ± 1.10	-12.01 ± 1.38	-25.54 ± 1.01
80024	B8[b]	6.12 ± 0.78	-11.89 ± 1.01	-24.25 ± 0.71
80062	B9.5 Va[c]	9.82 ± 2.44	-17.31 ± 2.88	-19.40 ± 2.08
80063	A0[d]	7.45 ± 3.42	-17.55 ± 4.17	-13.24 ± 2.86

Notes. Parallaxes and proper motions are taken from van Leeuwen (2007).

[a] Hernández et al. (2005).

[b] Strictly, kB8HeA0hB8IImA2IbSi(Cr:) (Garrison & Gray 1994).

[c] HIP 80062/63 form a visual double (Gray et al. 2006).

[d] kA0hA0VmA2 (Abt et al. 1979).

A.6. OphN 5

The OphN 5 field contains no mass above $A_V > 10$ and no YSOcs. The dark cloud L1752 is centered further to the east. OphN 5 is also associated with ^{13}CO cloud C (Nozawa et al. 1991) but no C^{18}O core (Tachihara et al. 2000b).

A.7. OphN 6

OphN 6 is associated with the L1719 dark cloud and two high extinction regions, Tachihara et al.'s (2000b) C^{18}O cores a (south) and b (north), and contains two Class III YSOcs and one flat-spectrum source (YSOc8). YSOc7, associated with IRAS 16186−1953, is probably a background giant due to its proper motions (see Section 3.5). YSOc7 is variable in the optical/near-infrared; the DENIS Consortium (2005) reports variation of more than a magnitude in I and J bands. YSOc8 is associated with IRAS 16191−1936. OphN YSOc9 has a small 24 μm excess and was previously unknown. The YSOcs lie away from the extinction peaks, but two lie on the edges of high extinction regions: Class III YSOc7/IRAS 16186−1953 in the south and the flat-spectrum YSOc8 at the edge of the northern extinction peak.

The flat-spectrum source YSOc8 is associated with L1719B and has a CO outflow (Bontemps et al. 1996). The submm emission is still uncertain: while there is a 220 mJy detection at 1.3 mm suggesting a disk mass of 0.04 Msun (André & Montmerle 1994; Andrews & Williams 2007), SCUBA observations only give an 850 μm upper limit of 54 mJy beam^{-1} (Kirk et al. 2005). Weak submm emission was detected with SCUBA toward L1719D at $16^{\rm h}21^{\rm m}09^{\rm s}.2{-}20^{\circ}07'10''$ with a flux of 62 mJy beam^{-1}. These weak emission SCUBA jiggle maps do not reproduce well as contours and are not shown in Figure 10; see Kirk et al. (2005) for images.

OphN 6 hosts two of the MIPS+2MASS identified YSOcs: M3 and M4. Both of these have proper motions consistent with Ophiuchus distances (Roeser et al. 2010). M4 lies 9″ away and within the positional errors of *ROSAT* X-ray source 2RXP J162230.1−200256, supporting its identification as a YSO.

The bright region in the southwest of OphN 6 contains four late-type B/early A stars: HIP 80019, HIP 80024, and HIP 80062/3. The revised *Hipparcos* parallaxes (van Leeuwen 2007) and *Tycho-2* proper motions for these stars are given in Table 11. The weighted mean of the four parallaxes gives a distance of 164^{+18}_{-15} pc, larger than our assumed 130 pc (equivalent to a parallax of 7.4 mas) but consistent with parallax distances for other stars illuminating nebulae in the vicinity of Sco/Oph (Mamajek 2008) and with distance estimates for Upper Sco (145 ± 2 pc; de Zeeuw et al. 1999). The proper motions are also similar to each other and consistent with membership of Upper Sco (Mamajek 2008; Hoogerwerf & Blaauw 2000). Three of these stars are clearly associated with the cloud through nebulae (see the three-color images and 24 μm emission, Figures 2, 3, and 10). HIP 80019 has no apparent nebula. HIP 80062/3, a wide B9 binary with HIP 80063 itself a close binary, illuminate the optically visible reflection nebula IC4601 (Magakian 2003).

It is not yet clear if these stars are pre-main sequence. None of them have the red colors characteristic of YSOs with disks (Figure 5 and 7). Neither HIP 80019 nor 80024 show emission lines characteristic of Herbig AeBe stars (Hernández et al. 2005). However, Dahm & Carpenter (2009) found a small excess above 10 μm for HIP 80024 in *Spitzer* spectroscopy and characterized this source as a debris disk with the proviso that they "cannot rule out that the dust is remnant primordial material." This star lies outside the region mapped at 24 μm in our study so we can neither confirm nor deny this disk excess. The two stars HIP 80062/63 driving IC4601 would be interesting targets for further studies now that their revised *Hipparcos* parallaxes and *Tycho-2* proper motions are consistent with membership of Upper Sco.

The bright star saturated in the IRAC bands at $16^{\rm h}20^{\rm m}20\overset{\rm s}{.}9$–$20^\circ08'05''$ is identified as 2MASS J16202094−2008059, and also saturated in 2MASS H and K_S. It is not obviously associated with any local nebulosity and, given its extremely red colors ($V - K \sim 10$; Zacharias et al. 2005), is probably a background giant.

A.8. CB68

The CB68 globule (L146) contains a well-studied isolated Class 0 object, from the *IRAS* faint source catalog IRAS 16544−1604. The associated submm emission is bright and extended 40″ in size with peak flux densities of 2.1 and 0.42 Jy beam^{-1} at 450 and 850 μm, respectively, and an estimated mass of 0.1 $M_\odot$ (Huard et al. 1999; Vallée et al. 2003; Young et al. 2006). The molecular core is elongated northeast-southwest, with a perpendicular molecular outflow detected in ^{12}CO (Vallée et al. 2000, 2003). The dust emission shows strong (11%) polarization yielding an estimated magnetic field strength of 120–130 μG in the radial direction Vallée & Fiege (2007). CB68 also has a C^{18}O detection (Nozawa et al. 1991 ^{13}CO core 34) though the Tachihara et al. (2000b) C^{18}O core q2 lies 0.4 degrees farther to the north.

CB68 has more than one associated source in the *Spitzer* catalog, as shown in Figure 14. The main source YSOc10 is strongly detected by IRAC and MIPS. A very red SED, with no 2MASS detections and rising toward 100 μm, confirms the Class 0 status (Figure 6). To the southeast, 15″ away, a second source is detected by IRAC. This lies within the point spread of MIPS emission from the central source, is bandfilled at 24 μm, and also shows some MUXBLEED artifacts to the north. From its SED, this source is a star (Figure 14) and though its MIPS flux is uncertain due to the confusion with IRAS 16544−1604 there is no evidence for a disk excess. At 15″ to the southeast, it has no associated 450 μm emission. All four IRAC bands show the outflow cavity extending to the northwest (Figure 14). There is also nebulosity to the west and east in the 3.6 and 4.5 μm bands.

IRAS 16534−1557 lies 15 arcmin to the northwest of CB68. This source is associated with Lee & Myers (1999) core 224 or Tachihara et al. (2000b) core q2 (see Figure 2 in Vallée & Fiege 2007) and has a rising *IRAS* spectrum characteristic of a YSO (Carballo et al. 1992), but lies beyond the range of our *Spitzer* map.

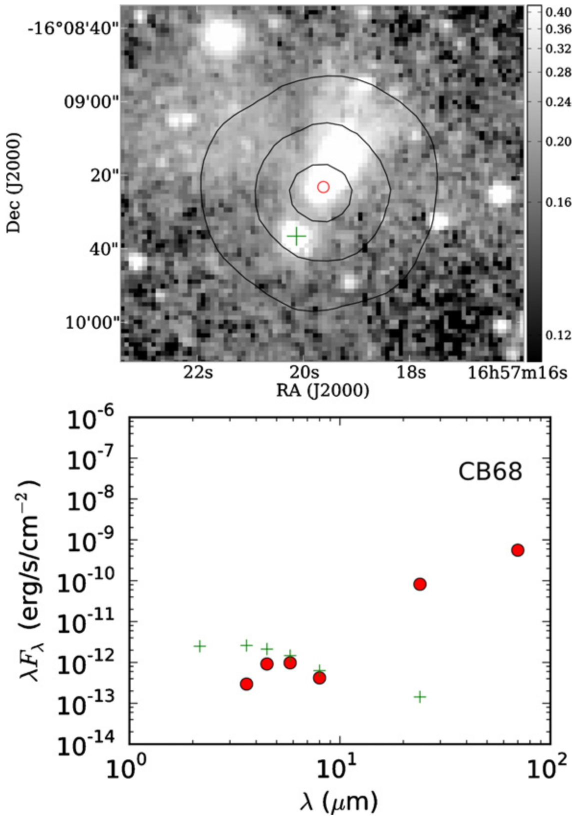

Figure 14. Top: CB68 imaged by IRAC 2 (4.5 μm) showing the reflection nebula extending toward the northwest in the direction of the outflow. The black contours are MIPS 70 μm [50, 100, 500] MJy sr^{-1}. Markers show the YSOc (circle, red in the online version) and southern star (+, green in the online version) from the *Spitzer* catalog. Bottom: CB68 SEDs for the YSO (circles) and the confusing star to the southeast (+).

(A color version of this figure is available in the online journal.)

REFERENCES

Abt, H. A., Brodzik, D., & Schaefer, B. 1979, PASP, 91, 176
André, P., & Montmerle, T. 1994, ApJ, 420, 837
Andrews, S. M., & Williams, J. P. 2007, ApJ, 671, 1800
Andrews, S. M., Wilner, D. J., Hughes, A. M., Qi, C., & Dullemond, C. P. 2009, ApJ, 700, 1502
Bontemps, S., André, P., Terebey, S., & Cabrit, S. 1996, A&A, 311, 858
Calvet, N., & Gullbring, E. 1998, ApJ, 509, 802
Cao, Y., Terebey, S., Prince, T. A., & Beichman, C. A. 1997, ApJS, 111, 387
Carballo, R., Wesselius, P. R., & Whittet, D. C. B. 1992, A&A, 262, 106
Cardelli, J. A., Clayton, G. C., & Mathis, J. S. 1989, ApJ, 345, 245
Chapman, N. L., Mundy, L. G., Lai, S.-P., & Evans, N. J. 2009, ApJ, 690, 496
Chen, J.-H., Evans, N. J., II, Lee, J.-E., & Bourke, T. L. 2009, ApJ, 705, 1160
Clemens, D. P., & Barvainis, R. 1988, ApJS, 68, 257
Dahm, S. E., & Carpenter, J. M. 2009, AJ, 137, 4024
de Geus, E. J. 1992, A&A, 262, 258
de Geus, E. J., Bronfman, L., & Thaddeus, P. 1990, A&A, 231, 137
de Geus, E. J., de Zeeuw, P. T., & Lub, J. 1989, A&A, 216, 44
DENIS Consortium 2005, The DENIS Database, VizieR Online Data Catalog: B/denis
de Zeeuw, P. T., Hoogerwerf, R., de Bruijne, J. H. J., Brown, A. G. A., & Blaauw, A. 1999, AJ, 117, 354
Di Francesco, J., Johnstone, D., Kirk, H., MacKenzie, T., & Ledwosinska, E. 2008, ApJS, 175, 277
Dobashi, K., Uehara, H., Kandori, R., et al. 2005, PASJ, 57, 1
Ducourant, C., Teixeira, R., Périé, J. P., et al. 2005, A&A, 438, 769
Evans, N. J., II, Allen, L. E., Blake, G. A., et al. 2003, PASP, 115, 965
Evans, N. J., II, Dunham, M. M., Jørgensen, J. K., et al. 2009, ApJS, 181, 321
Evans, N. J., II, Harvey, P. M., Dunham, M., et al. 2007, Final Delivery of Data from the c2d Legacy Project: IRAC and MIPS, Technical Report (Pasadena, CA: Spitzer Science Center), http://irsa.ipac.caltech.edu/data/SPITZER/C2D/doc/c2d_del_document.pdf
Fazio, G. G., Hora, J. L., Allen, L. E., et al. 2004, ApJS, 154, 10

Flagey, N., Noriega-Crespo, A., Boulanger, F., et al. 2009, ApJ, 701, 1450
Froebrich, D., Ray, T. P., Murphy, G. C., & Scholz, A. 2005, A&A, 432, L67
Garrison, R. F., & Gray, R. O. 1994, AJ, 107, 1556
Gray, R. O., Corbally, C. J., Garrison, R. F., et al. 2006, AJ, 132, 161
Greene, T. P., Wilking, B. A., André, P., Young, E. T., & Lada, C. J. 1994, ApJ, 434, 614
Gutermuth, R. A., Bourke, T. L., Allen, L. E., et al. 2008, ApJ, 673, L151
Han, F., Mao, R. Q., Lu, J., et al. 1998, A&AS, 127, 181
Hartmann, L., Megeath, S. T., Allen, L., et al. 2005, ApJ, 629, 881
Harvey, P., Merín, B., Huard, T. L., et al. 2007, ApJ, 663, 1149
Harvey, P. M., Chapman, N., Lai, S., et al. 2006, ApJ, 644, 307
Harvey, P. M., Huard, T. L., Jørgensen, J. K., et al. 2008, ApJ, 680, 495
Hatchell, J., Fuller, G. A., Richer, J. S., Harries, T. J., & Ladd, E. F. 2007, A&A, 468, 1009
Heiderman, A., Evans, N. J., II, Allen, L. E., Huard, T., & Heyer, M. 2010, ApJ, 723, 1019
Hernández, J., Calvet, N., Hartmann, L., et al. 2005, AJ, 129, 856
Hoogerwerf, R., & Blaauw, A. 2000, A&A, 360, 391
Huard, T. L., Sandell, G., & Weintraub, D. A. 1999, ApJ, 526, 833
Indebetouw, R., Mathis, J. S., Babler, B. L., et al. 2005, ApJ, 619, 931
Ishihara, D., Kaneda, H., Onaka, T., et al. 2011, A&A, 534, 79
Jones, D. H., Peterson, B. A., Colless, M., & Saunders, W. 2006, MNRAS, 369, 25
Kirk, J. M., Ward-Thompson, D., & André, P. 2005, MNRAS, 360, 1506
Kirk, J. M., Ward-Thompson, D., Di Francesco, J., et al. 2009, ApJS, 185, 198
Koresko, C. D. 2002, AJ, 124, 1082
Lee, C. W., & Myers, P. C. 1999, ApJS, 123, 233
Loren, R. B. 1989, ApJ, 338, 902
Lynds, B. T. 1962, ApJS, 7, 1
Magakian, T. Y. 2003, A&A, 399, 141
Mamajek, E. E. 2008, Astron. Nachr., 329, 10
Megeath, S. T., Allgaier, E., Young, E., et al. 2009, AJ, 137, 4072
Merín, B., Jørgensen, J., Spezzi, L., et al. 2008, ApJS, 177, 551
MIPS Instrument Support Teams 2007, MIPS Instrument Handbook V3.3 (Pasadena, CA: SSC)
Mizuno, A., Onishi, T., Yonekura, Y., et al. 1995, ApJ, 445, L161
Nozawa, S., Mizuno, A., Teshima, Y., Ogawa, H., & Fukui, Y. 1991, ApJS, 77, 647
Nutter, D., Ward-Thompson, D., & André, P. 2006, MNRAS, 368, 1833
Oliveira, I., Merín, B., Pontoppidan, K. M., et al. 2009, ApJ, 691, 672
Ossenkopf, V., & Henning, T. 1994, A&A, 291, 943
Padgett, D. L., Rebull, L. M., Stapelfeldt, K. R., et al. 2008, ApJ, 672, 1013
Parker, N. D. 1991, MNRAS, 251, 63
Peterson, D. E., Caratti o Garatti, A., Bourke, T. L., et al. 2011, ApJS, 194, 43
Pojmanski, G., Pilecki, B., & Szczygiel, D. 2005, Acta Astron., 55, 275
Rebull, L. M., Padgett, D. L., McCabe, C., et al. 2010, ApJS, 186, 259
Rebull, L. M., Stapelfeldt, K. R., Evans, N. J., II, et al. 2007, ApJS, 171, 447
Reipurth, B., & Zinnecker, H. 1993, A&A, 278, 81
Rieke, G. H., Young, E. T., Engelbracht, C. W., et al. 2004, ApJS, 154, 25
Robitaille, T. P., Meade, M. R., Babler, B. L., et al. 2008, AJ, 136, 2413
Roeser, S., Demleitner, M., & Schilbach, E. 2010, AJ, 139, 2440
Rowles, J., & Froebrich, D. 2009, MNRAS, 395, 1640
Schechter, P. L., Mateo, M., & Saha, A. 1993, PASP, 105, 1342
Skrutskie, M. F., Cutri, R. M., Stiening, R., et al. 2006, AJ, 131, 1163
Spezzi, L., Vernazza, P., Merín, B., et al. 2011, ApJ, 730, 65
Straizys, V. 1984, Vilnius Astronomijos Observatorijos Biuletenis, 67, 3
Tachihara, K., Abe, R., Onishi, T., Mizuno, A., & Fukui, Y. 2000a, PASJ, 52, 1147
Tachihara, K., Dobashi, K., Mizuno, A., Ogawa, H., & Fukui, Y. 1996, PASJ, 48, 489
Tachihara, K., Mizuno, A., & Fukui, Y. 2000b, ApJ, 528, 817
Tachihara, K., Onishi, T., Mizuno, A., & Fukui, Y. 2002, A&A, 385, 909
Terebey, S., Fich, M., Noriega-Crespo, A., et al. 2009, ApJ, 696, 1918
Vallée, J. P., Bastien, P., & Greaves, J. S. 2000, ApJ, 542, 352
Vallée, J. P., & Fiege, J. D. 2007, AJ, 134, 628
Vallée, J. P., Greaves, J. S., & Fiege, J. D. 2003, ApJ, 588, 910
van Leeuwen, F. 2007, A&A, 474, 653
Visser, A. E., Richer, J. S., & Chandler, C. J. 2001, MNRAS, 323, 257
Visser, A. E., Richer, J. S., & Chandler, C. J. 2002, AJ, 124, 2756
Wainscoat, R. J., Cohen, M., Volk, K., Walker, H. J., & Schwartz, D. E. 1992, ApJS, 83, 111
Ward-Thompson, D., André, P., Crutcher, R., et al. 2007, in An Observational Perspective of Low-Mass Dense Cores II: Evolution Toward the Initial Mass Function, ed. B. Reipurth, D. Jewitt, & K. Keil (Tucson, AZ: Univ. Arizona Press), 33
Weingartner, J. C., & Draine, B. T. 2001, ApJ, 548, 296
Whitney, B. A., Sewilo, M., Indebetouw, R., et al. 2008, AJ, 136, 18
Wilking, B. A., Gagné, M., & Allen, L. E. 2008, in Handbook of Star Forming Regions, Volume II, ed. B. Reipurth (San Francisco, CA: ASP), 351
Wright, E. L., Eisenhardt, P. R. M., Mainzer, A. K., et al. 2010, AJ, 140, 1868
Young, C. H., Bourke, T. L., Young, K. E., et al. 2006, AJ, 132, 1998
Zacharias, N., Monet, D. G., Levine, S. E., et al. 2005, VizieR Online Data Catalog, 1297, 0